Aspects Of Auditory Signal Transduction

DIPLOMARBEIT

der Fakultät für Biologie

der EBERHARD KARLS UNIVERSITÄT TÜBINGEN

vorgelegt von

Henninger, Jörg

Tübingen, Juni 2008

Eigenständigkeitserklärung

Hiermit erkläre ich, dass ich diese Arbeit selbst verfasst und keine anderen als die angegebenen Quellen und Hilfsmittel benutzt habe.

Tübingen, den 16.06.2008

Jörg Henninger

Der Kampf gegen Gipfel vermag ein Menschenherz auszufüllen. Wir müssen uns Sisyphos als einen glücklichen Menschen vorstellen.

Albert Camus, *Der Mythos des Sisyphos*

Contents

Acknowledgements

This work would not have been possible without the help and support of many people. Special thanks goes to my supervisor, Jan Benda. Most of all, for venturing the experiment of letting an applied biologist do a theoretical thesis. His persistent encouragement and patience as well as his willingness to give me room to follow my own ideas prepared the ideal ground for my work.

Also, I would like to thank Andrea Stith for reading the manuscript and giving me invaluable advice concerning the English language. If this work is smooth and easy to read, the credits are hers.

The ITB was a great place for my work and enjoyed the discussions and beneficial influence of the ITB people. I'm very grateful to Andreas Herz for giving me the opportunity to work in his group. No work would have been possible without the appropriate infrastructure. And so, I would like to thank Andreas Hantschmann for guiding me through the obstacles of the Linux-environment and helping me out whenever it was necessary.

Last, but not least, I'm very grateful to all of my friends, who eased the negative effects of intensive work by welcome distraction. Especially, I would like to thank Noemi Barnet, who persistently encouraged and supported me in many ways.

CHAPTER 1

INTRODUCTION

All organisms live in an environment full of changes, full, as it has been said, of 'happenings' (Smith, 2000). Some of these changes will be beneficial to the organism, others detrimental. The fullest possible knowledge of relevant 'happenings' underlies the organisms ability to adapt to its environment. Thus, *sensory perception* of environmental stimuli is a fundamental characteristic of all living organisms and is of utmost importance for survival. Highly sophisticated sensory systems for a large panoply of physical stimuli have evolved (Hudspeth and Logothetis, 2000), and each sensory system is tuned to a specific type of stimulus, termed *adequate stimulus*. The major types of sensory systems are mechanoreceptors, chemoreceptors and photoreceptors, although more exotic receptor types such as electroreceptors and magnetoreceptors have evolved as well. In animals neural sensory systems developed that connect the sensory perception to the animal's nervous system. Thus, sensory perception in animals is a *transduction* of a certain physical stimulus into an electrical signal that can be processed by its nervous system. The transduction is accomplished by receptor cells, which *transform* a physical stimulus step by step into the *stimulus representation*. The transformation of each step defines the relationship between the stimulus and the response of the sensory receptor. The succession of each individual step forms a *signal transduction chain*. As more is known about the biophysical structure of a sensory system on a molecular and anatomical level, more emphasis is placed on its functional characteristics. These can be recognized as a critical level of biological organization (Hartwell et al., 1999) and offers the means to connect molecular biology to emergent phenomena.

Neural Basics Neural systems are composed of neuronal cells, called neurons. Alike all biological cells, neurons exhibit a negative voltage potential across their cell membrane. Neurons utilize changes of this membrane potential to process and convey information. The steady-state of the membrane potential is dependent on the types and amounts of ions inside and outside the cell as well as on conductivity of the cell membrane to these ions. Relevant ions usually are potassium, sodium and chloride. The specific composition of inner and outer fluids is strongly dependend on the specific cell type and organism. The conductivity of the cell membrane is controlled by the presence of specialized ion-channels. Specialized structures of neurons process and convey the information stored in the membrane potential actively and for this purpose feature voltage-dependent ion-channels that possess dynamic opening properties. The opening state, better, the opening probability of these voltage-dependent ion-channels is associated with the membrane potential.

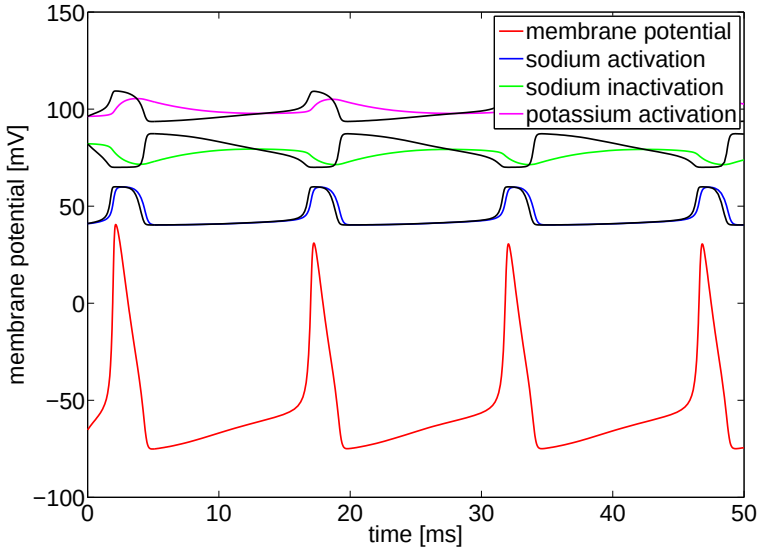

Figure 1.1: HODGKIN-HUXLEY MODEL. Time course of the membrane potential and gating parameters due to constant input. Gating parameters are shifted and displayed without axis. Figure adapted from Hodgkin and Huxley (1952a,b,c,d).

There are many types of neurons and each type exhibits a complex anatomy, the characteristics of which adapt the neuron to its individual function. Despite the anatomical complexity and functional variety of neuronal cells, there are common features. These are the neuron's *soma*, which comprises the cell nucleus, the *dendrite*, which typically receives the cell's main excitatory input and the *axon*, which conveys the processed information to other cells. Excitatory inputs are typically depolarising and inhibitory inputs hyperpolarizing. Typically, the axon and the so-called 'axon hill' (the region of the soma where the axon originates) feature the voltage-dependent ion-channels described earlier. When the membrane potential at the axon hill exceeds a certain threshold, a so-called *action potential* is evoked in an all-or-nothing fashion. The details of the underlying processes that cause this particular response have been unraveled and described by the unprecedented work of Hodgkin and Huxley (Hodgkin and Huxley, 1952a,b,c,d). The properties of the mathematical model is shown in Figure (1.1). Due to the particular response behaviour of voltage-dependent ion-channels, the axon hill can be recognized as the site of signal integration, where incoming signals from the dendrite are processed. Other regions of the neuron, e.g. the dendrite, exhibit passive *electrotonic* transduction properties only.

Passive Membrane Properties The thin and isolating cell membrane divides well conducting compartments and thus acts as an electric condensator, whose capacity is found to be uniformly $1\,\mu\text{F/cm}^2$ in all cells examined so far (Gentet et al., 2000), due to the homogenous structure of the lipid double layer. If a constant current step with amplitude I_0 is injected into a small and isopotential patch of passive neuronal membrane, the charge flows into the capacitance and the potential rises starting at $V_m(0) = 0$

$$V_m(t) = V_\infty(1 - e^{-t/\tau_m}), \tag{1.1}$$

with the membrane time constant $\tau_m = C_m R_m$, where C_m is the specific membrane capacitance (in μF cm^{-2}) and R_m the specific membrane resistance (in $\Omega\,\mathrm{cm}^2$). This time course is governed by exponential decay toward the steady-state $V_\infty = R_m I_0$. Thus, in one time constant ($t = \tau$) the electrotonic potential will reach 63 % of V_∞. The estimates of τ_m are known to depend heavily on the experimental conditions, i.e. the composition of the physiological solution and the quality of the seal. For a full review, see Zigmond et al. (1999).

1.1 Auditory Transduction and Mechanoreceptors

The process of hearing captures acoustic information that is embedded in rapid pressure fluctuations of a medium. Accordingly, auditory sensory organs are found to be composed of mechanically resonating structures that are driven by the sound-waves and conjuncted mechanosensitive (auditory) receptor cells, which convert the induced oscillations of the resonators in electrical signals. A huge variety of resonating structures such as eardrums, basilar membranes and hair sensilla have evolved (Robles and Ruggero, 2001; French, 1988; Martin C. Göpfert, 2002). The oscillations cause mechanosensory ion-channels to open (Hudspeth, 1985; Hill, 1983; Gillespie and Walker, 2001) and thereby induce a depolarising transduction current. The transduction current accumulates and charges the membrane. A *receptor potential* builds up and either directly evokes action potentials in the receptor cell or is transmitted to other cells.

Most information in sound is contained in its temporal structure. To be able to extract the behaviourally relevant information, the temporal resolution of auditory system must be as fine as the relevant structures of the stimulus. This attribute makes the auditory system particularly well suited for the study of time processing in nervous systems. The time resolution is not by far limited by the width of an action potential, as has been shown by several examples (Mason, Oshinsky, and Hoy, 2001; Knudsen, 1980; Neuweiler and Schmidt, 1993), where resolutions of a few microseconds are achieved. The ability of auditory receptor cells to read out stimuli with high temporal resolution often finds its correspondence in the temporal accuracy of the response.

Auditory systems have developed in a huge variety in animals, but common features exist. Typically, the stimulus space of sound comprises a much higher dimensionality than the response space of the receptor neuron. Hence, auditory transduction process involves a *dimensional reduction* that can be interpreted as *stimulus integration*. The auditory transduction process is based on the recognition of oscillation structures and, therefore, on mechanosensitive ion-channels in the receptor cells. These channels are very scarce (Hudspeth, 1989; Gillespie, 1995) and many details about them are unknown. Transduction is rapid and, thus, no second messengers can be involved (Hudspeth and Logothetis, 2000; Gillespie and Walker, 2001). Furthermore, mechanoperception is evolutionarily old and is found as the basis for different senses in all kinds of organisms. Hence, evolutionary relationships can be suspected (Martinac, 2001).

1.2 Anatomy of the Locust Auditory System

Gollisch et al. performed studies on the auditory periphery of the migratory locust (*Locusta migratoria* L., Orthoptera, Acrididae). The physiology of hearing in locusts is less complex than in mammals and has been well described (Gray, 1960; Michelsen, 1971a; Stephen and Bennet-Clark, 1982; Jacobs, Otte, and Lakes-Harlan, 1999). The basic structure is highly conserved

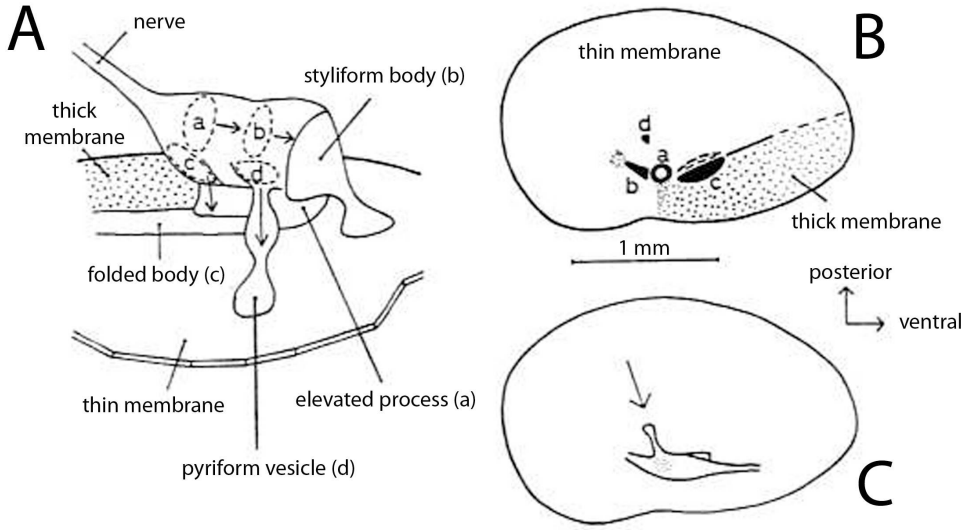

Figure 1.2: SCHEMATA OF THE TYMPANUM AND AUDITORY GANGLION OF THE LOCUST *Schistocerca gregaria*. (A) The auditory ganglion (Müller's organ) is attached directly to the tympanum. Four branches (a-d) project to different attachment sites of the tympanum that possess different resonance characteristics. (B) Attachment sites (a-d) of the tympanum. The structure of the tympanum is heterogenic. Thick and thin parts of the tympanum are indicated and correspond to different resonance frequencies. (C) Location of the Müller's organ on the tympanum. The arrow indicates the viewing angle for panel A. Figure taken from Michelsen (1971a).

across locust species. Still, the coupling of receptor cells to an eardrum suggests functional similarities to the mammalian ear. Locust possess two ears, located in the first abdominal segment, just above the coxa of the hindlegs, where the leg is attached at each side of the body. Both ears are connected by a cavity that allows air-pressure to pass through the animals body and, thus, locust ears act as pressure-difference receiver for low sound frequencies. The resonance structure of each ear is a heterogenic structured tympanum. Attached to the inner side of the tympanum is the auditory ganglion (Müller's organ), which contains the somata of 60-80 receptor cells (1.2).

The auditory receptor cells of locusts are chordotonal organs, which are commonly used in insects for mechanoperception. Chordotonal organs are composed of scolopodia (Fig. 1.3A) that contain a single primary (neuronal) receptor cell (Fig. 1.3B). The dendrites of the receptor cells project to four different attachment sites of the tympanum each exhibiting different resonance characteristics. The receptor cell's dendrites are approximately 100 µm long and are enclosed by satellite cells. The dendrites don't branch and contain a single cilium that protrudes from its apex and connects to the hypodermis of the tympanum. Physiological classification due to sensitivity maxima and absolute sensitivities of the receptor neurons yields three (Jacobs et al., 1999) to four functional groups (Michelson, 1971). However, receptor cells exhibit characteristic frequencies of about 5 kHz in *low-frequency receptor cells*, or of about 15 kHz in *high-frequency receptor cells*. The tuning properties are obtained from the local resonance characteristics of the tympanum (Fig. 1.2B) and, thus, resemble a *place coding* similar to those of vertebrate ears. The receptor cell's axons project to the metathoracic ganglion. In order to keep the auditory periphery intact, electrophysiological measurements were performed at a distal position of the axonal projection.

In comparison to the mammalian ear, locust ears are structurally simple. The mammalian cochlea possesses complex mechanical properties, including feedback loops and nonlinear amplification (Martin and Hudspeth, 1999; Eguíluz, Ospeck, Choe, Hudspeth, and Magnasco,

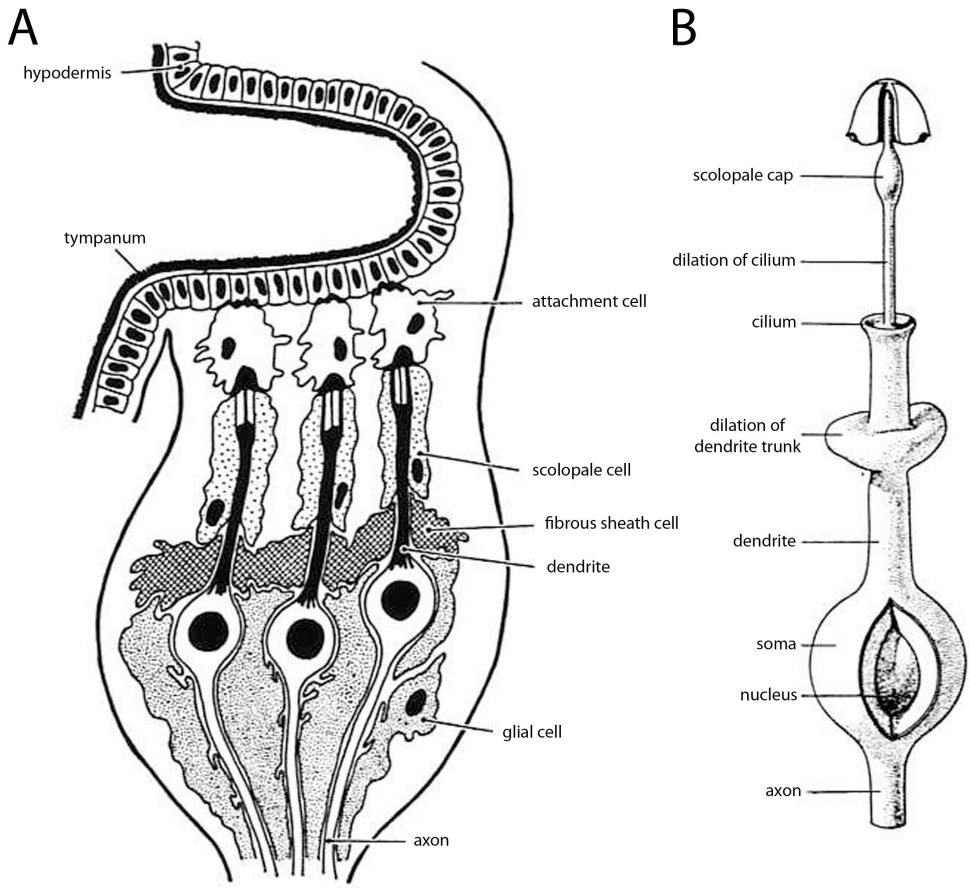

Figure 1.3: ANATOMY OF AUDITORY RECEPTORS CONNECTED TO A FOLD OF THE TYMPANUM OF THE LOCUST *Schistocerca gregaria*. (A) Chordotonal organ in the auditory ganglion. Chordotonal organs are central building blocks of auditory receptors in insects. Each organ consists of specialized sensilla known as scolopidia. Each scolopidium consists of one or more neurosensory cells from whose dendrite a sensory cilium originates. The receptor neurons are surrounded by satellite cells - glial cells, fibrous sheath cells, and scolopale cells. The distal segment of the dendrite is enclosed within an attachment cell and the whole attached to a cap cell. The cap cell in turn connects to the tympanum. (B) Dendritic structure of a receptor neuron. Dendrite and cilium display particular dilations whose function and relevance for transduction is unknown. Figure taken from Gray (1960).

2000), which seem to be absent in locust auditory receptors. However, measurements of otoacoustic emissions indicate small nonlinear effects in locust ears, too (Kössl and Boyan, 1998). Mammalian *hair cells*, are secondary (non-neuronal) auditory receptors that convey the receptor potential via synapses to auditory-nerve fibers. However, sound transduction in mammalian and insect ears conceptually involves the same sequence of procceses. Thus, functional insights gained from the investigation of the locust auditory system is likely to be beneficial for the functional understanding of mammalian hearing.

1.3 Iso Response Method

Central to this thesis is the indirect analysis of transduction with iso-response methods as introduced by Gollisch, Schütze, Benda, and Herz (2002); Gollisch and Herz (2005), as well as by the dissertation of Gollisch (2004).

The periphery of the locust auditory system is delicate and vulnerable, and *in vivo* investigations of auditory signal transduction need to minimize the impact on the site of transduction in order to yield reliable results. This calls for indirect methods, so that the mechanical structures of the ear remain intact. The auditory transduction chain is a sequence of processes transforming the acoustic input into a series of action potentials. This computation, as it is performed by auditory receptor neurons, is characterized by *functional* modules. Prior knowledge of the system's basic structure, given by its biophysical composition, may act as a guide to the development of a model framework (a so called *cascade model*) to identify the functional modules. Such an approach may be referred to as a *gray-box*. Typical elements of cascade models are *temporal linear filters* and *static nonlinear transformations*. A characteristic of a temporal linear filter is that it uses stimulus contributions from different time points to determine the final output.

What do we know about the auditory signal transduction chain in the locust? From the transduction chain's physical structure, we can assume a step-by-step conversion of the incoming signal. First, air-pressure fluctuations of the sound wave drive an oscillation of the mechanical resonator, the eardrum. These oscillations are hypothesized to induce the opening of mechanosensitive ion channels in the apical dendritic membrane of the auditory receptor neurons. The opening of the ion channels leads to transduction currents which cause a generator potential over the cell's membrane. Eventually, such a generator potential activates voltage-dependent ion channels that trigger action potentials, once a certain threshold is reached.

In this sequence of processes, at least two potentially nonlinear transformations can be identified. (1) The gating-process and (2) the transformation of an electrical potential into a sequence of all-or-nothing action potentials. Commonly used techniques provided by nonlinear systems theory for the analysis of cascade models are limited to cascades with only a single nonlinear transformation. Another issue of many classical approaches is the limited temporal resolution, when the system's output is jittered by noise. In case of the auditory system the spike jitter (about 1 ms) smooths out the temporal correlation between input and output and hence, the temporal resolution needed to analyze auditory systems (about 10 µs) can't be achieved.

An alternative approach to this problem is the iso-response method. It extends an experimental strategy well known from the measuring of tuning curves in psychophysics and the measuring of threshold curves in neurobiology: the application of 'equivalence criteria' to analyze a certain system. Central to this method is the identification of sets of different stimuli that cause the same response. These *iso-response sets* (IRS) are subsets of the stimulus space and characterize the invariances of the system. A classical example for the measurement of

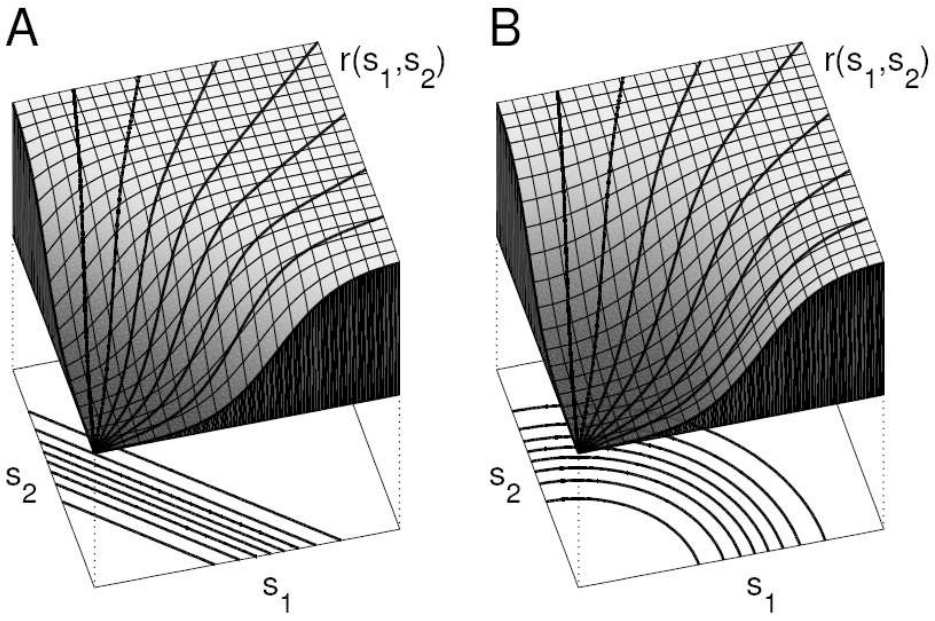

Figure 1.4: EFFECT OF AN INPUT NONLINEARITY IN AN NLN CASCADE. The responses of two models to the two-dimensional stimulus space (defined by stimuli s_1 and s_2) are compared. The first model (A, Eq. 1.2) takes the linear sum and the second model the quadratic sum (B, Eq. 1.3) as an argument of a sigmoidal nonlinear output function. The surface plots of the model's response functions $r(s_1, s_2)$ are similarly shaped and the response functions $r(s_1)$ and $r(s_2)$ are even identical. However, the contour lines (iso-response sets) of the systems clearly differ and reveal the input nonlinearity. Figure taken from Gollisch et al. (2002).

iso-response sets comes from psychophysics: so called 'isophones' are curves that identify the identically perceived loudness of a tone in respect to it's frequency and sound-pressure-level.

Here, this method will be used to analyze the locust auditory transduction chain. Neurons perform a *reduction* of the high-dimensional stimulus space to a lower dimensional output. While the sensory system can be driven by a wide range of possible stimuli, $s(t)$, consisting of a set of components, $s_1, s_2, ..., s_n$, the system's response is limited to a lower-dimensional output function $r(s(t))$. In the simplest case, the response would be described as a one-dimensional variable r, representing, e.g., a firing rate of spikes or a 'spike probability' of a single sensory receptor neuron. The method is complemented by a mathematical cascade-model framework. A cascade model describes the transformations performed by a signal processing system (e.g., a receptor neuron) as a sequence of filter functions. To understand this approach, we begin with an example. We compare two signal processing systems with only two input components s_1 and s_2. The first model is an LN-cascade, where a linear function, L, is followed by an output nonlinearity, N, which is represented by a filter function $g(\cdot)$. The second model is an NLN-cascade, which contains an additional quadratic input nonlinearity, so that the linear function is sandwiched between two nonlinearities. The output nonlinearities are $g(x) = \tanh(x)$ for the first model and $g(x) = \tanh(\sqrt{x})$ for the second. We obtain the form of the two models as

$$r_1(s_1, s_2) = \tanh(s_1 + s_2), \tag{1.2}$$

$$r_2(s_1, s_2) = \tanh\left(\sqrt{s_1^2 + s_2^2}\right). \tag{1.3}$$

If only a single input component is presented, the two models will show identical responses. The square root in model two cancels the square of the input nonlinearity and nothing is revealed about the input nonlinearity. The responses of these models to two input components

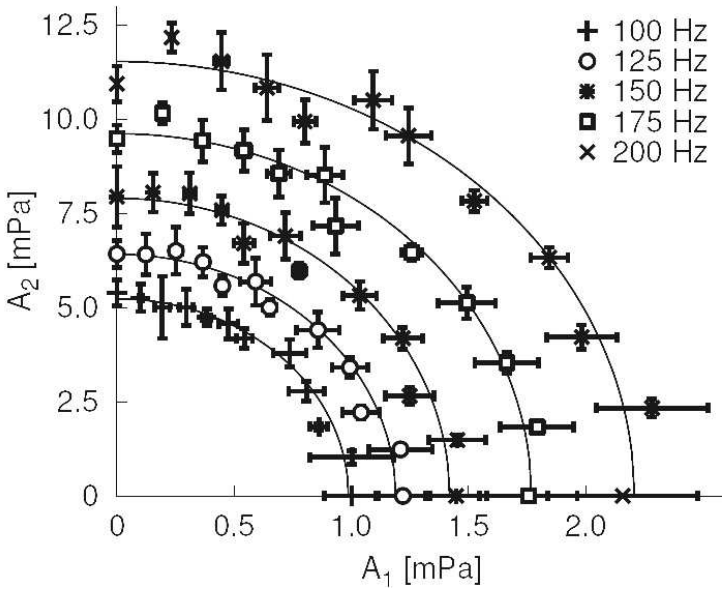

Figure 1.5: ISO-RESPONSE SETS FOR SUPERPOSITIONS OF TWO PURE TONES FROM ONE RECEPTOR CELL AT DIFFERENT FIRING RATES. Stimuli composed of superpositions of two pure sine tones with amplitudes A_1 and A_2 are tuned to yield the same output firing rate as indicated. Measuring multiple ratios A_1/A_2, specifically shaped curves in stimulus space were obtained that reveal information about the underlying integration process. The solid lines are ellipses fitted to the data and indicate a static quadratic nonlinearity. Note the different scales of A_1 and A_2. These are due to the differential response of the system to different frequencies, that are in accordance with frequency tuning-curves of the locust's auditory receptor. Figure taken from Gollisch et al., 2002.

look very similar in surface plots (Fig. 1.4) and any measurement along a radial direction will produce sigmoidal response curves similar to the response of those with only a single input component. But the projections of the contour lines below the response surfaces reveal how such nonlinearities can be determined experimentally. While the first model produces straight contour lines, those of the second model are segments of circles. The difference of these projections is clearly and easily distinguishable in experiments and can thus be used to identify the character of input nonlinearities. Any arbitrary contour line represents a certain output level and thus corresponds to an iso-response set. For each iso-response set the input parameters are tuned to yield the same level of response. This identical response is the reason why this method is independent of the specific shape of the output nonlinearity, provided the output function is monotonic. The application of such an analysis in an experimental situation can be achieved by fixing all but one degree of freedom of a stimulus and tune the remaining free parameter until the desired response is achieved. This free parameter then defines the direction of search for iso-response stimuli.

1.4 Analysis of the Auditory Signal Transduction Chain

1.4.1 What does the Receptor Neuron measure?

The receptor neuron is a measuring device that could possibly measure different qualities of sound. In order to distinguish between several hypothesis, an investigation of the mechanism underlying spectral integration has been performed (Fig. 1.5, Gollisch et al., 2002). For this purpose iso-response sets for superpositions of long pure tones were measured and three hypothesis were examined experimentally. It was tested whether the amplitude, the energy or

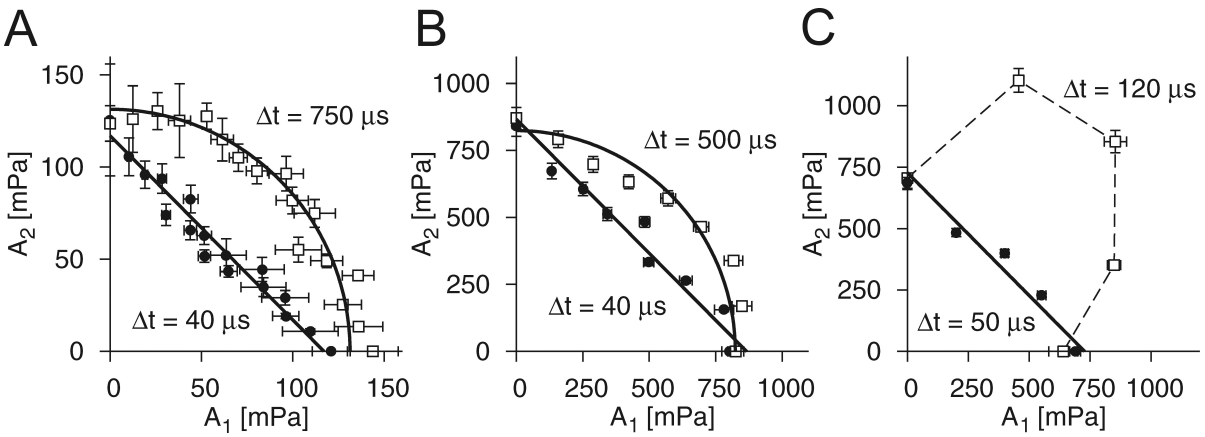

Figure 1.6: ISO-RESPONSE SETS FOR TWO-CLICK STIMULI AND IDENTIFICATION OF RELEVANT STIMULUS PARAMETERS. Two short clicks, separated by an interclick interval Δt, were presented for multiple fixed amplitude ratios A_1/A_2 and simultaneously tuned to yield the same spike probability $p = 70\%$. Each panel shows results for a single cell and iso-response sets for two different interclick intervals Δt. Iso-response sets display specific shapes for short and long inter-click times Δt. For short Δt (40 and 50 µs, A-C) iso-response sets are well described as straight lines, for long Δt (500 and 750 µs, A-B) iso-response sets are well described by segments of circles. Intermediate Δt (120 µs, C) are stronger bulged and don't fit either scheme. This behaviour is interpreted as two different processes that govern stimulus integration at short and long time scales, which might overlap for intermediate time scales. Thus, for short Δt the sound-pressure seems to be the relevant stimulus parameter, while for long Δt the sound energy is the relevant stimulus parameter. Figure taken from Gollisch and Herz (2005)

the sound pressure determines the response of the receptor neuron. The approach presented in Section 1.3 was applied and stimuli composed of two pure sine tones with fixed and unequal frequencies, ω_1 and ω_2, were presented:

$$s(t) = A_1 \sin(\omega_1 t) \; + \; A_2 \sin(\omega_2 t). \tag{1.4}$$

Measurements were performed for multiple amplitude ratios A_1/A_2, which were kept fixed for each measurement and simultaneously tuned to yield the same output firing rate as the receptor neuron. Since a constant output level indicates a constant input into the spike generator, the output nonlinearity can be neglected. This characteristic is the key feature of the iso-response method, because it allows to treat an LNLN-cascade model mathematically as an LNL-cascade model. Each hypothesis corresponds to a specific shape of iso-response curves. According to the amplitude hypothesis, iso-response curves are straight lines; according to the energy hypothesis, they are ellipses; and according to the pressure hypothesis, they are even more strongly bent curves, whose exact shape has to be determined numerically. The measured iso-response curves for different output firing rates (Fig. 1.5) are found to be described best by ellipses, a strong evidence that the square of the amplitudes is added. These results correspond to the energy hypothesis since the square of the amplitude is proportional to the energy of sound waves.

1.4.2 Temporal Integration

Experiments with long, stationary stimuli are well suited to examine static nonlinearities of the auditory system. Because dynamics of temporal integration occur on shorter time scales, they are averaged out by this type of experiment. Hence, for investigating temporal integration in receptor neurons another type of experiment is needed . Furthermore, long, stationary stimuli don't correspond well to the situation in a natural environment, where often quick fluctuations in

the amplitude and frequency of sound waves convey important information that enables organisms to perform tasks such as sound localization, echolocation and communication. To capture this information, auditory systems must be able to follow these rapid changes, and thus, fine temporal resolution can be expected. Little is known about the temporal characteristics of auditory systems on short time scales. To investigate these processes, iso-response sets with short, temporally structured stimuli were designed (Gollisch and Herz, 2005).

The core building blocks of these experiments were short sound-pressure pulses with a width of 20 μs, called *clicks*. These clicks were combined in pairs of two and are separated by a peak-to-peak interval, Δt, in order to examine the signal cascade for input nonlinearities on different time scales. The stimulus space is thus parameterized by the click amplitudes, A_1 and A_2, while Δt defines the time scale of the experiment. The response of the receptor neurons to such stimuli is at most one action potential per double click. A firing rate is an inadequate description of response strength and thus the spike probability, p, was used instead. While stimulus intensity hardly influenced spike timing, it had strong influence on spike probability. Measurements were performed for multiple repetitions for the same stimulus and the average number of action potentials per trial was taken to yield p.

Similar to the experiments introduced in the previous Section, stimuli consisting of pairs of clicks with fixed amplitude ratios, A_1/A_2, were tuned simultaneously to yield the same predefined spike probability of $p = 70\%$. Again, iso-response sets are measured for multiples ratios A_1/A_2 and different peak-to-peak intervals Δt (Fig. 1.6). The shapes of the iso-response sets vary systematically with Δt. For short interclick intervals (40 μs) iso-response sets exhibit straight lines, while for long interclick intervals ellipses are obtained. Sets of intermediate Δt (120 μs) don't fall in either of these categories, but show a particular bulged shape. These results indicate that at least two different processes govern signal processing on different time scales. On short time scales a linear summation of the clicks causes iso-response sets with straight lines and indicate that sound pressure is the relevant stimulus parameter here. This is not suprising as the first known step in auditory signal transduction is the deflection of the eardrum. Because of the mechanical inertia of this structure, superposition of quick following clicks can be expected. On longer time scales the quadratic sum governs the response and thus the sound energy is the relevant stimulus parameter. Thus, two different summation processes exist, which are separated by a static quadratic nonlinearity. Biophysically, the second summation is assumed to occur at the neural membrane, where electrical charge accumulates. This is supported by the findings that the DC component of the membrane potential in hair cells is proportional to sound energy (Dallos, 1985).

1.4.3 The Cascade Model

With this knowledge, a model for the auditory transduction for pulse-like click stimuli has been suggested (Gollisch and Herz, 2005). As a first step, the tympanic oscillation is caused by the first click, with a deflection proportional to the amplitude A_1. The change in the membrane potential is then proportional to A_1^2, due to the static quadratic nonlinearity. After the interclick interval, Δt, the second click will add to the tympanic oscillation and to the membrane potential. But as some time Δt has passed, both the deflection of the tympanic oscillation as well as the membrane potential have changed in dependence of Δt. These changes are described as filter functions $L(\Delta t)$ for the tympanic oscillation and $Q(\Delta t)$ for the membrane potential. Therefore at time Δt the deflection of the tympanum is $A_1 \cdot L(\Delta t)$ and the membrane potential is $A_1^2 \cdot Q(\Delta t)$. The second click at time Δt adds it's amplitude A_2 to the tympanic oscillation, yielding $A_1 \cdot L(\Delta t) + A_2$, and thus changes the membrane potential with $[A_1 \cdot L(\Delta t) + A_2]^2$,

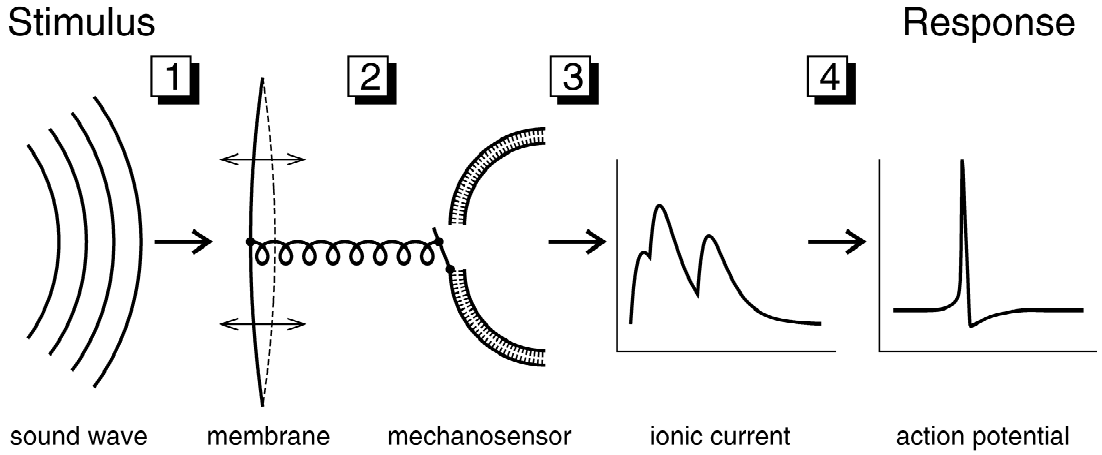

Figure 1.7: SEQUENTIAL PROCESSING IN THE AUDITORY TRANSDUCTION CHAIN. Sound stimuli are encoded into a neural spike response by a series of biophysical transformations. Sound-pressure waves deflect a mechanical oscillatory component (1, mechanical coupling) like the tympanic membrane, which is supposed to be linked to ion-channels in the receptor cell's apical membrane. The deflection causes the ion-channels to open, a transduction current is induced (2, mechanosensory transduction) and charges up the membrane potential (3, electrical integration). Voltage-dependent ion-channels are activated and action potentials are triggered once a certain threshold is reached (4, spike generation). The first and third step are approximated by linear, while the gating mechanism is well described by a static quadratic nonlinearity and the spike generation is known to comprise a static nonlinear, sigmoidal shape. Figure taken from Gollisch and Herz (2005)

considering the squaring of the oscillatory component. Therefore, we obtain an effective stimulus strength, $J(\Delta t)$, where

$$J(\Delta t) = A_1^2 \cdot Q(\Delta t) \; + \; [A_1 \cdot L(\Delta t) \; + \; A_2]^2 . \tag{1.5}$$

This effective stimulus strength $J(\Delta t)$ will be transformed into a spike probability p by the final static nonlinearity $g(J(\Delta t)) = p$, which describes the nonlinear transformation of the spike generator. The obtained signal processing chain has the form of an LNLN-cascade. The possible biophysical mechanisms underlying of the auditory transduction chain are displayed in Figure 1.7.

The Generalized Cascade Model

The corresponding LNLN cascade, which is not limited to click stimuli, is presented in Figure 1.8. The input to the general model is a time-dependent sound-pressure wave A(t). The components of the general LNLN cascade model are four model steps (with the causality condition $\tau > 0$):

1. convolution with a linear filter $l(\tau) = \sin(\omega\tau)e^{-\delta\tau}$
2. squaring
3. convolution with a linear filter $q(\tau) = e^{-\lambda\tau}$, yielding the effective sound intensity $J(t)$
4. application of a nonlinear transformation $\tilde{g}(J)$.

The response $r(t)$ is thus given by

$$r(t) = \tilde{g}(J(t)). \tag{1.6}$$

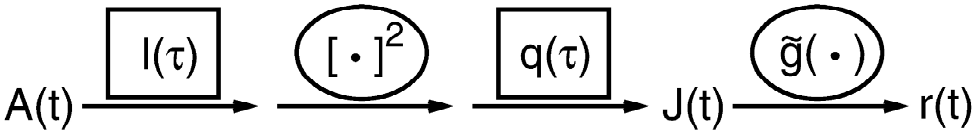

Figure 1.8: GENERALIZED CASCADE MODEL OF THE AUDITORY TRANSDUCTION CHAIN. The linear temporal filters $l(\tau), q(\tau)$ and the squaring nonlinearity transform the sound-pressure wave $A(t)$ into the effective stimulus strength $J(t)$. Finally the nonlinearity $\tilde{g}(\cdot)$, which may differ from the nonlinearity $g(\cdot)$ of the click-version, transforms $J(t)$ into the neural response $r(t)$. Figure taken from Gollisch et al., 2005.

1.4.4 Temporal Characteristics of Stimulus Integration

The Equation 1.5 offers a direct way to obtain the filter functions $L(\Delta t)$ and $Q(\Delta t)$ by comparison of iso-response sets with conveniently chosen stimuli. Although the effects of these two filter functions may largely overlap, it is possible to distinguish between them. As we are dealing with two unknowns, we need two equations for each Δt to be able to calculate solutions for both unknowns. Equation 1.5 indicates that any pair of clicks (B_1, B_2) at a fixed time Δt should yield the same spike probability p as the pair (A_1, A_2) when $J(A_1, A_2) = J(B_1, B_2)$. For each Δt two different patterns of paired clicks are used for iso-response sets. In the first pattern, the second click is presented in the same direction as the first click (amplitude A_2, "positive") and in the opposite direction in the second pattern (amplitude $\tilde{A}_2$, "negative"). The first click, A_1, is held positive in all measurements. Because both patterns of stimuli are tuned to yield the same spike probability p, this implies that $J(t)$ is equal in both instances. As derived in Gollisch and Herz (2005), only a small part of $J(t)$ contributes to the spike probability, p. Therefore, we will refer to the effective stimuli intensity by the term J from here on. Let us note that amplitudes A_2 and $\tilde{A}_2$ used here are the *absolute values of these amplitudes* and we get

$$J = A_1^2 \cdot Q(\Delta t) + [A_1 \cdot L(\Delta t) + A_2]^2 \tag{1.7}$$

$$J = A_1^2 \cdot Q(\Delta t) + \left[A_1 \cdot L(\Delta t) - \tilde{A}_2\right]^2 \tag{1.8}$$

Setting the two right sides equal to each other, we obtain

$$[A_1 \cdot L(\Delta t) + A_2]^2 = \left[A_1 \cdot L(\Delta t) - \tilde{A}_2\right]^2 \tag{1.9}$$

with the solution

$$L(\Delta t) = \frac{\tilde{A}_2 - A_2}{2A_1} \tag{1.10}$$

for the first linear filter. Inserting $L(\Delta t)$ into (1.7), we get for the second linear filter

$$Q(\Delta t) - c = -\left(\frac{\tilde{A}_2 + A_2}{2A_1}\right)^2, \tag{1.11}$$

with $c = J/A_1^2$, which can be left as a free parameter. Measurements for different values of Δt make it possible to extract the whole time course of $L(\Delta t)$ and $Q(\Delta t)$, as shown in Figure 1.9. The possible temporal resolution of this approach is much higher than that of traditional approaches of nonlinear system analysis, because it is not limited by the precision of the output, rather only by the precesion of the input. The function $L(\Delta t)$ is interpreted as the oscillation of the tympanum at the attachment site of the receptor cell. The function $Q(\Delta t)$ is interpreted as the electrical integration and the decay time constant is interpreted as the membrane time

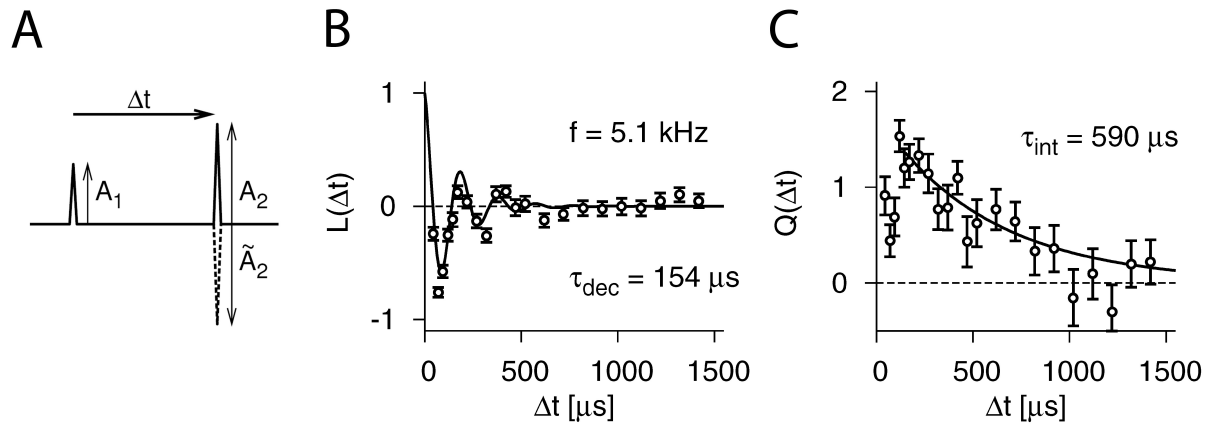

Figure 1.9: TEMPORAL STRUCTURE OF THE MECHANICAL OSCILLATION AND ELECTRICAL INTEGRATION. (A) For the measurement of the filter functions $L(\Delta t)$ and $Q(\Delta t)$, two different patterns of stimuli were used. For each pattern, two clicks were presented, separated by a interclick interval Δt. While the first click (amplitude A_1) was always held positive, the second click was presented in either the same (amplitude A_2, "positive") or the opposite (amplitude $\tilde{A}_2$, "negative") direction of A_1. (B) Time course of the eardrum vibration, calculated as $L(\Delta t)$, of a low-frequency receptor neuron. The frequency is obtained by comparison with a damped harmonic oscillation (C) Time course of the electrical integration process. Decay time is obtained by comparison with an exponential decay function. Figure taken from Gollisch et al., 2005.

constant. The latter was found to be in the range of 200 to 800 µs. These values are by at least one order of magnitude smaller than membrane time constants of typical neurons.

The calculation above derives solutions for $L(\Delta t)$ and $Q(\Delta t)$ for click experiments, without explaining explicitly what these filter functions mean. The relationships of these functions and the functions $l(\Delta t)$ and $q(\Delta t)$ of the general cascade model (Section 1.4.3,Fig. 1.8) are explained in detail in the appendix of Gollisch and Herz (2005). It is derived that $L(\Delta t)$ is identical to a phase shifted form of $l(\Delta t)$, which may be interpreted as the velocity of the eardrum. It may also be interpreted as the temporal change of the eardrum's movement. The relationship between $Q(\Delta t)$ and $q(\Delta t)$ is more complicated.

In this work, we investigate this relationship and ask which parts of the spike generator might be measured by $Q(\Delta t)$. Subsequently, we explore possible interpretations of our findings.

CHAPTER 2

SEQUENCED FILTERS

2.1 Linear Filters and Convolution

Sequences of filter functions play an important role in the description of signal cascades and are mathematically treated as convolutions of these filter functions. Often, filter functions in signal transduction chains comprise an exponentially decaying component. For this reason, we introduce here the basic properties of convolutions with respect to sequences of exponential decay functions. The time course of the exponential decay functions, investigated here, depends on *time constants*, τ_i, which can either delay or accelerate the convergence of the functions to zero.

A sequence of filter functions results in an 'overall filter function' that inherits its characteristics by the individual filter functions. This overall filter function is identical to the convolution of all sequenced filter functions. The results of the convolutions can also be understood in a physical sense: they would then correspond to the *impulse response* of the sequenced filters to a very short impulse.

We are particularly interested in how the time constants of the single filter functions influence the overall filter function. Furthermore, we ask how well the time constants of the individual filter functions describe characteristics of the overall filter function.

2.1.1 Convolution of Two Exponential Filter Functions

The convolution of two functions $f(t)$ and $g(t)$ is defined as

$$(f*g)(t) = \int_{-\infty}^{\infty} f(\lambda)\, g(t-\lambda)\, d\lambda. \tag{2.1}$$

Convolutions are commutative and associative, so the order of the convolution steps is insignificant. Following Eq. (2.1), the convolution of two exponential functions

$$f(t) = \Theta(t)\cdot\exp(-t/\tau_1) \quad \text{and} \quad g(t) = \Theta(t)\cdot\exp(-t/\tau_2),$$

with time constants τ_1 and τ_2, will be

$$(f*g)(t) = \int_{-\infty}^{+\infty} \Theta(\lambda)\, e^{-\frac{\lambda}{\tau_1}}\, \Theta(t-\lambda)\, e^{-\frac{t-\lambda}{\tau_2}}\, d\lambda \;=\; \int_0^t e^{-\frac{\lambda}{\tau_1}} e^{-\frac{t-\lambda}{\tau_2}}\, d\lambda, \tag{2.2}$$

where $\Theta(t)$ is the Heavyside function: $\Theta(t) = 1$ for $t > 0$ and $\Theta(t) = 0$ for $t < 0$.

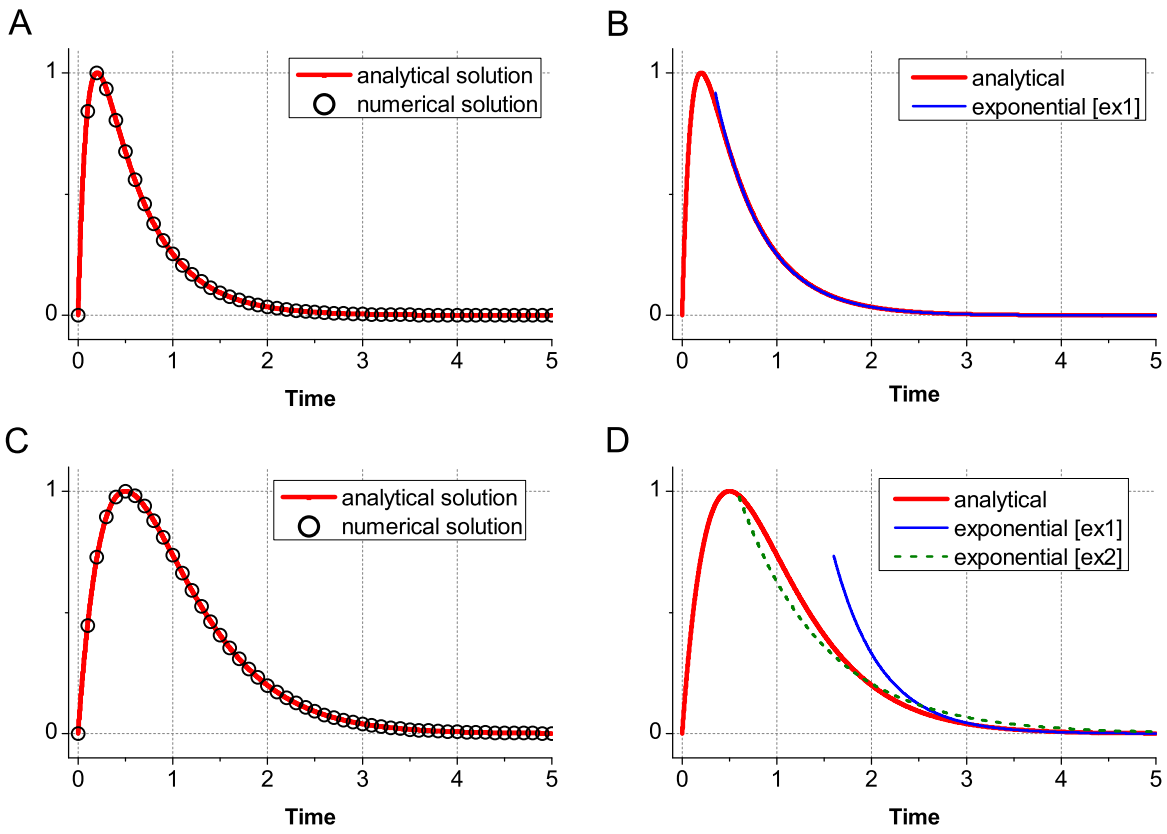

Figure 2.1: CONVOLUTIONS. Two exponential decay functions with time constants τ_1 and τ_2 are convolved and the analytical and numerical results are compared for the cases $\tau_1 \neq \tau_2$ (A,B, Eq. 2.4) and $\tau_1 = \tau_2$ (C,D, Eq. 2.6). The tails of the results are matched manually with exponential decay functions to extract a single time constant describing the tail.
(A,B) $\tau_1 = 0.1$ and $\tau_2 = 0.5$. Due to the significant difference of the time constants, the tail of the overall filter function is well described by the longer time constant (ex1, $\tau = 0.5$). (C,D) $\tau_1 = \tau_2 = 0.5$. The tail of the overall filter function is not well described by the input time constant (ex1, $\tau = 0.5$) . If such a sequence with similar time constants would be analyzed by fitting the tail with an exponential decay function, it is likely that the time constant is overestimated (ex2, $\tau = 0.9$).

1. If $\tau_1 \neq \tau_2$, we get

$$\int_0^t e^{-\frac{\lambda}{\tau_1}} e^{-\frac{t-\lambda}{\tau_2}}\, d\lambda = e^{-\frac{t}{\tau_2}} \left[\frac{\tau_1\tau_2}{\tau_1-\tau_2}\, e^{-\lambda\frac{\tau_2-\tau_1}{\tau_1\tau_2}} - e^{-\frac{t}{\tau_2}} \right]_0^t \tag{2.3}$$

$$= \frac{\tau_1\tau_2}{\tau_1-\tau_2} \left[e^{-\frac{t}{\tau_1}} - e^{-\frac{t}{\tau_2}} \right], \tag{2.4}$$

which is a difference of two exponentials, multiplied by a constant factor. The shape of the resulting function changed due to the substraction: unlike an exponential decay function, the new function rises initially from zero to reach a peak and then converges to zero again. If the time constants differ greatly in scale, e.g. $\tau_1 \ll \tau_2$, the initial rise will be short and the tail will be well described by the longer time constant (Fig. 2.1B), since $\exp(-t/\tau_1)$ will converge much faster to zero than $\exp(-t/\tau_2)$. But as the time scales become more similar, the overall filter function will better resemble the second case:

2. For $\tau_1 = \tau_2 = \tau$, we find the solution

$$\int_0^t e^{-\frac{\lambda}{\tau_1}} e^{-\frac{t-\lambda}{\tau_2}}\, d\lambda = e^{-\frac{t}{\tau}} \int_0^t e^{-\lambda\cdot 0}\, d\lambda \tag{2.5}$$

$$= t\cdot e^{-\frac{t}{\tau}}. \tag{2.6}$$

Although this solution is not a difference of exponential functions, the basic shape of this result is similar to the first case (Fig. 2.1C). However, the tail of the overall filter function is not well described by the input time constant τ, since the factor t in Eq. (2.6) increases with time $t \to \infty$ and by this distorts $\exp(-t/\tau)$. In Figure (2.1D) we added a second manually matched exponential decay function, *ex*2. We demonstrate that the overall time course of the tail is much better described by a time constant much greater than those of the convolved filter functions.

2.1.2 Convolution of Three Exponential Filter Functions

We now perform a convolution of these results with a third exponential filter function with time constant τ_3,

$$h(t) = \Theta(t)\ \cdot exp(-t/\tau_3). \tag{2.7}$$

1. For $\tau_1 \neq \tau_2 \neq \tau_3$, we obtain from Eq. 2.4

$$(f*g*h)(t) = \int_0^t a\cdot \left[e^{-\frac{\lambda}{\tau_1}} - e^{-\frac{\lambda}{\tau_2}} \right] e^{-\frac{t-\lambda}{\tau_3}}\, d\lambda \tag{2.8}$$

$$= a\cdot b\cdot \left[e^{-\frac{t}{\tau_1}} - e^{-\frac{t}{\tau_3}} \right] - a\cdot c\cdot \left[e^{-\frac{t}{\tau_2}} - e^{-\frac{t}{\tau_3}} \right], \tag{2.9}$$

with constants $a = \frac{\tau_1\tau_2}{\tau_1-\tau_2}$, $b = \frac{\tau_1\tau_3}{\tau_1-\tau_3}$ and $c = \frac{\tau_2\tau_3}{\tau_2-\tau_3}$.

2. For $\tau_1 = \tau_2 = \tau \neq \tau_3$ we get

$$(f*g*h)(t) = \left[\frac{\tau\tau_3}{\tau_3-\tau} \right]^2 \cdot \left[e^{-\frac{t}{\tau_3}} - e^{-\frac{t}{\tau}} - t\cdot \frac{\tau_3-\tau}{\tau_3\tau}\cdot e^{-\frac{t}{\tau}} \right]. \tag{2.10}$$

Both (1) and (2) are differences of exponentials again and thus show similar shape and characteristics as the first case we discussed (Fig. 2.2A,C). Again, when the longest time constant differs greatly from the other time constants, the tail of the overall filter function is well described by an exponential decay function with the longest of the three time constants. (Fig. 2.2B,D).

3. For $\tau_1 = \tau_2 = \tau_3 = \tau$, we get

$$(f * g * h)(t) = \frac{1}{2} t^2 \cdot e^{-\frac{t}{\tau}}. \tag{2.11}$$

While the basic shape remains the same, a broadening of the overall filter function results and the description of the tail by an exponential decay function with the time constant τ worsens, since the factor t^2 in Eq. (2.11) increases with time $t \to \infty$ and by this distorts $\exp(-t/\tau)$. In Figure (2.1D) we added a second manually matched exponential decay function, *ex*2. We demonstrate that the overall time course of the tail is much better described by a time constant much greater than those of the convolved filter functions.

For the case of n convolved filter functions, f^n, with $\tau_i = \tau$ and $1 \leq i \leq n$, we find the solution for the overall function

$$f^n = \frac{1}{(n-1)!}\, t^{n-1} \cdot e^{-\frac{t}{\tau}} \tag{2.12}$$

2.1.3 Shifting of the Peak

We address the relationship between the shift of the peak and the time constants of the involved filters. For this we again consider the two cases, (1) $\tau_1 = \tau_2 = \tau$ and (2) $\tau_1 \neq \tau_2$ separately.

1. For $\tau_1 = \tau_2 = \tau$. At the maximum the derivative of Eq. (2.6) vanishes and we get

$$\frac{d}{dt}\left[t \cdot e^{-\frac{t}{\tau}}\right] = e^{-\frac{t}{\tau}} \cdot \left[1 - \frac{t}{\tau}\right] = 0. \tag{2.13}$$

Thus, the maximum occurs, at $t_{peak} = \tau$.

For the case of n convolved filter functions, f^n, with $\tau_i = \tau \; \forall 1 \leq i \leq n$, we find the derivative

$$\frac{d}{dt} f^n = \frac{1}{(n-2)!}\, t^{n-2}\, e^{-\frac{t}{\tau}} \left(1 - \frac{1}{\tau\, n}\, t\right) \tag{2.14}$$

Here, the maximum occurs, at $t_{peak} = \tau\,(n-1)$. Thus, the more filter are contained in the sequence, the later the peak occurs.

2. For $\tau_1 \neq \tau_2$. The derivative of Eq. (2.4) is

$$\frac{d}{dt}\left[e^{-\frac{t}{\tau_1}} - e^{-\frac{t}{\tau_2}}\right] = -\frac{1}{\tau_1} \cdot e^{-\frac{t}{\tau_1}} + \frac{1}{\tau_2} \cdot e^{-\frac{t}{\tau_2}} = 0. \tag{2.15}$$

Since this equation cannot be solved analytically, we hypothesize that Eq. (2.15) is true for $t_{peak} \approx \tau_1 + \tau_2$. We then find that

$$e^{-1}\left[-\frac{1}{\tau_1} e^{-\frac{\tau_2}{\tau_1}} + \frac{1}{\tau_2} e^{-\frac{\tau_1}{\tau_2}}\right] \approx 0. \tag{2.16}$$

This equation is true in the limit of $\tau_1 \to \infty$ and $\tau_2 \to \infty$, and thus the peak is indeed at $t_{peak} = \tau_1 + \tau_2$

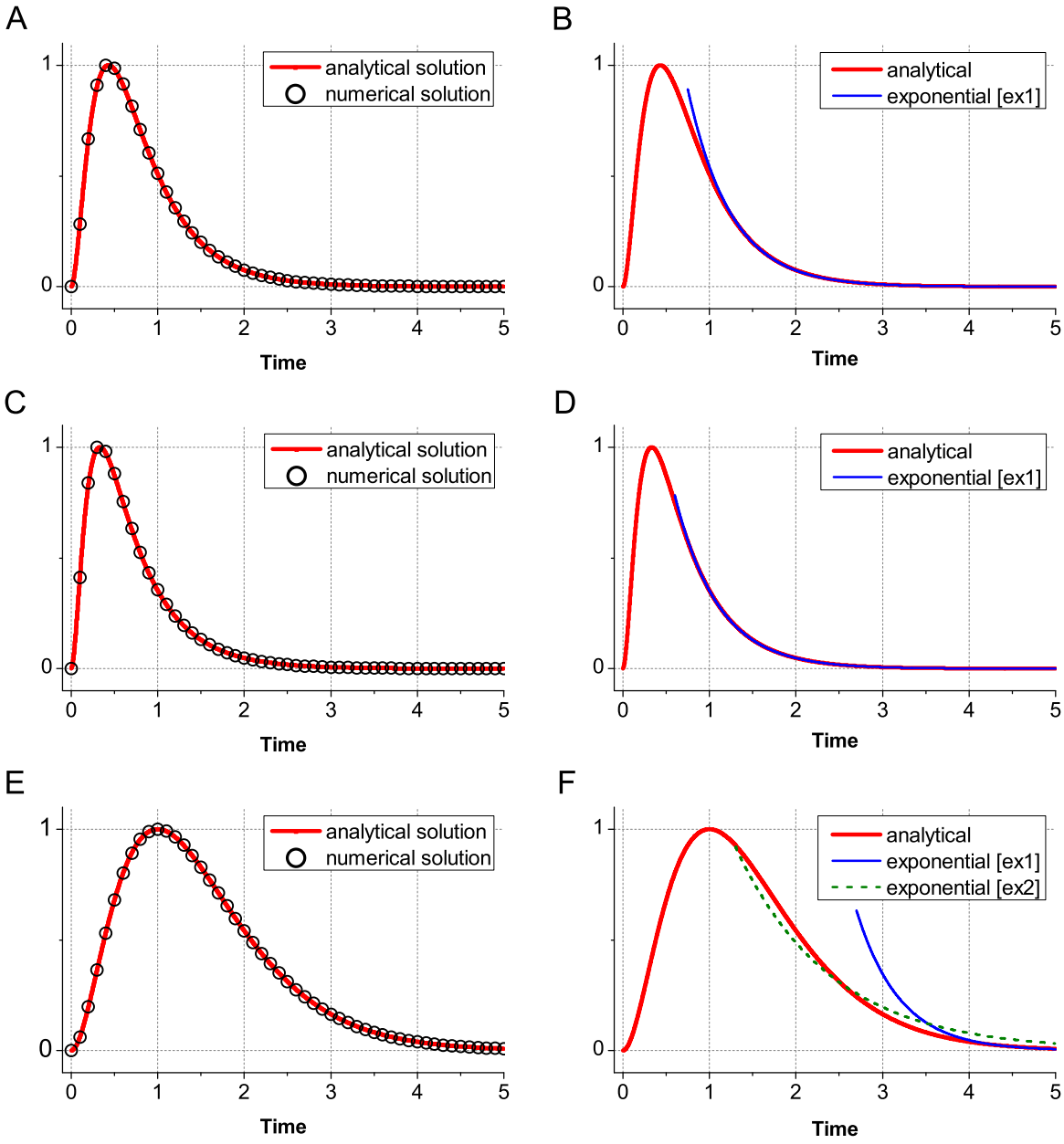

Figure 2.2: CONVOLUTIONS. Three exponential decay functions with time constants $\tau_{1,2,3}$ are convolved and the analytical and numerical results are compared for the cases $\tau_1 \neq \tau_2 \neq \tau_3$ (A,B, Eq. 2.9), $\tau_1 = \tau_2 \neq \tau_3$ (C,D, Eq. 2.10) and $\tau_1 = \tau_2 = \tau_3$ (E,F, Eq. 2.11). The tails of the results are matched manually with exponential decay functions to extract a single time constant describing the tail.
(A,B) $\tau_1 = 0.1, \tau_2 = 0.2$ and $\tau_3 = 0.5$. Due to the strong difference of the time constants, the overall filter function is well described by the longer time constant (ex1, $\tau = 0.5$). (C,D) $\tau_1 = \tau_2 = 0.1$ and $\tau_3 = 0.5$. Again, the overall filter function is well described by the longest time constant (ex1, $\tau = 0.5$). (E,F) $\tau_1 = \tau_2 = \tau_3 = 0.5$. The tail of the overall filter function can't be well described by the input time constant (ex1, $\tau = 0.5$). If such a sequence with similar time constants were analyzed by fitting the tail with an exponential decay function, it is likely that the time constant would be overestimated (ex2, $\tau = 1.1$).

Chapter Summary

In this Chapter, we learned that sequenced linear filters can be understood as convolutions the filter functions. We demonstrated that the longest time constant of the individual filter functions can be reliable extracted when the time constants differ greatly. We also demonstrated that the shape of the overall filter function is distorted when the individual time constants become similar. The overall shape is then better described by a time constant greater than those of the convolved filters.

CHAPTER 3

INTERPRETATION OF THE FILTER FUNCTIONS OBTAINED BY THE ISO-RESPONSE-METHOD

The iso-response sets (IRS) presented by Gollisch and Herz (2005) are a novel and powerful method to investigate sensory systems with a so far unprecedented high temporal resolution and without the need to corrupt the delicate and vulnerable sensory mechanism. As an indirect method the IRS returns the functional building blocks of the signal transduction cascade, $L(\Delta t)$ and $Q(\Delta t)$, which reflect the temporal characteristics of the eardrum vibration and the electrical integration at the cell membrane, respectively. What do we measure with $Q(\Delta t)$. We approach this question with simulations of the auditory transduction chain and a short review of the underlying mathematics. What characteristics of the spike-generator are captured by the IRS? To answer this question, we use different kinds of output functions. Are the conclusions drawn from previous experiments correct?

We begin our analysis with simulation of the first kind of iso-response sets, which utilizes pairs of click to extract the temporal structure of the filters $L(\Delta t)$ and $Q(\Delta t)$. We then examine the relationship between the measured filter $Q(\Delta t)$ and the actual impulse response of the model to a click impulse. Using different models as output functions, we approach the question, what characteristics of these output functions are captured by the iso-response sets. Additionally, we examine an alternative model for the general cascade, where we substitute the quadratic nonlinearity of the model by absolute values.

3.1 Numerical Simulations of IRS

In the introduction, we reviewed the structure of the generalized cascade model proposed for locust auditory transduction and the iso-response measurements, which are used to investigate the temporal structure of stimulus integration. Here, we reproduce these experiments by numerical simulations. To be able to calculate the two unknown filter functions $L(\Delta t)$ and $Q(\Delta t)$, two iso-response sets have to be measured for each interclick interval, Δt. While the first click is held constant in both set-ups, the second click is either presented in the same direction (first setup, amplitude A_2) or in the opposite direction (second setup, amplitude $\tilde{A}_2$) as the first click.

We perform a simulation of the distinct filter functions of the signal transduction chain, which

is modeled by

$$s(t) \xrightarrow{l(\tau)} \xrightarrow{[\cdot]^2} \xrightarrow{q(\tau)} Jt) \xrightarrow{\tilde{g}(\cdot)} p. \tag{3.1}$$

The linear filter functions are given by

$$l(\tau) = sin(\omega\tau)e^{-\frac{\tau}{\tau_{tymp}}}, \tag{3.2}$$

$$q(\tau) = e^{-\frac{\tau}{\tau_{int}}}, \tag{3.3}$$

with $\omega = 2\pi f$, the resonance frequency f and the time constants τ_{tymp} and τ_{int}. We model the eardrum as a damped harmonic oscillator, which is driven by input stimulus $s(t)$. It thus reads

$$s(t) = \ddot{x}(t) + \frac{2}{\tau_{tymp}}\dot{x}(t) + \omega^2 x(t), \tag{3.4}$$

This equation implements the first linear filter (Eq. 3.2). The output $x(t)$ is the deflection of the eardrum and is dimensionless. It is squared and used as input for the passive membrane equation, which has the general form

$$\tau_{int}\ \frac{d}{dt}\ V_m(t) = E - V_m(t) + R_{in}I(t), \tag{3.5}$$

with input $I(t) = x^2(t)$, input resistance $R_{in} = 1$, resting potential $E = 0$ and time constant τ_{int} of the electrical integration. We obtain

$$\tau_{int}\ \frac{d}{dt}\ V_m(t) = -V_m(t) + x^2(t) + D\cdot\xi, \tag{3.6}$$

with the gaussian white noise ξ and the noise-strength factor D. $V_m(t)$ is dimensionless. This component implements the second linear filter (Eq. 3.3) of the generalized cascade model (Eq. 3.1) and reflects the characteristics of the electrical integration process. The electrical integration is driven by $I(t) = x^2(t)$. For the spike generation we set a certain threshold, θ. When the voltage trace $V_m(t)$ exceeds the threshold a spike is evoked. This type of spike generation is known as a *leaky-integrate-and-fire neuron*. We are here using the probabilistic approach of Gollisch and Herz and, thus, need a spike probability, p, as output of the signal transduction chain. For that reason we added the gaussian noise to Equation 3.6. The standard deviation of the white noise was $D = 15\%$ of the threshold value, but the exact value is arbitrary. For each interclick interval Δt a sufficient number of trials has to be simulated to calculate an accurate spike-probability. The exact number of trials is dependent of the strength of the noise and can reach several thousand in order to obtain smooth curves.

It is possible to shorten this approach by calculating p directly instead of simulating a high number of trials. Therefore, we begin by calculating $V_m(t)$ by Eq. (3.6) without the noise term $D\cdot\xi$. White noise added to $V_m(t)$ follows a gaussian distribution around $V_m(t)$, as long as the voltage trace doesn't change too rapidly. Therefore, the probability that $V_m(t) + D\cdot\xi$ crosses the threshold at the time t can be calculated by an integral over the component of the tail of the error function, which exceeds the threshold. The transient point of the error function over the threshold, θ, is thereby given by $x = \theta - V_m(t)$. The integral can be conveniently calculated by the *complementary error function*. In our simulations, we are interested in the probability that a spike is evoked in a small time window, w, which is why we compute a second integral over the time span from times zero to w. The whole calculation is given by

$$g(J(t)) = p = \int_0^w dt\ \frac{1}{2}\ \text{erfc}\left[\frac{\theta - V_m(t)}{D\cdot\sqrt{2}}\right] \tag{3.7}$$

The calculation of the spike probability itself is a nonlinear process with a sigmoidal shape. We computed the spike probability $p(A_1, A_2)$ and $p(A_1, \tilde{A}_2)$, respectively, for each Δt.

For comparability and consistency of our simulations we choose the same parameter values for all of our models, if not mentioned explicitly elsewise. The tympanic membrane of the locust has a heterogenic structure and contains thick and thin areas (Fig. 1.2, Gray, 1960). This composition enables it to convey a broad spectrum of low and high frequencies, ranging up to at least 15 kHz. In correspondence to this and to experimental findings (Michelsen, 1971a; Jacobs et al., 1999), we choose a tympanal resonance frequency of $f = 4$ kHz for our modeled eardrum. In experiments, the tympanal decay time constant ranged between 100 to 250 µs. We here chose τ_{tymp} to be 200 µs. Furthermore, the experimental results indicate that the decay time constant of the electrical integration is ranging between 300 to 600 µs. We here chose τ_{int} to be 500 µs. Another parameter of importance is the width of our simulated sound-pressure-pulses. To be able to achieve a high temporal resolution we use very short pulses ('clicks') with a length of 10 µs and scan a range of interclick intervals from 0 to 3.5 ms in steps of 10 µs.

Figure 3.1A presents the absolute values of the amplitudes for the second click, denoted as A_2 if presented in the same direction as the first click, and $\tilde{A}_2$ if presented in the opposite direction. Each pair of stimuli (A_1, A_2) and $(A_1, \tilde{A}_2)$ is tuned such that the resulting spike probability is the same. The time courses of A_2 and $\tilde{A}_2$ display strong oscillatory components, reflecting the time course of the deflection of the tympanum. By means of Eq. 1.10 and 1.11 the filter functions $L(\Delta t)$ and $Q(\Delta t)$ are computed from A_2 and $\tilde{A}_2$ (Fig. 3.1B,C). The time course of $L(\Delta t)$ matches well the filter function

$$\tilde{l}(\Delta t) = e^{-\frac{t}{\tau_{tymp}}} \cdot \cos(\omega t), \tag{3.8}$$

which denotes a phase-shifted version of the filter $l(\Delta t)$ and describes the *change* of the eardrum vibration (Eq. 3.2). The time course of $Q(\Delta t)$ matches well with the filter function $q(\Delta t)$ of the electrical integration (Eq. 3.3).

3.2 Properties of the Filter Functions

These results demonstrate that the IRS effectively captures essential parameters of the linear filters before, $l(\Delta t)$, and after the quadratic nonlinearity, $q(\Delta t)$, as proposed by Gollisch and Herz (2005). Furthermore, the shapes of our calculated filter functions are very similar to the experimental results of Gollisch and Herz, shown in Figure (1.9). Note, that for small interclick intervals, $Q(\Delta t)$ shows strong oscillations, which are found in experimental results, too. These oscillations are not part of the modeled electrical integration (Eq. 3.6) or the filter function $q(\tau)$, respectively. Also, the oscillations can't be observed in the voltage trace of the model in response to a single click impulse (Figure 3.1D). This observations suggests that the oscillations are a characteristic trait of the iso-response method.

We possess full knowledge of all parameters in our simulation, including the time course of the tympanic vibration and electrical integration process, and are, hence, able to compare these with our results. Comparing the membrane potential and $Q(\Delta t)$, we find that $Q(\Delta t)$ seems to match well with a shifted form of the voltage trace of the model to a single click (Fig. 3.2). The required offset seems to equal the position of the peak of the voltage trace. Therefore, the iso-response method only reveals a part of the temporal integration at the receptor neuron's membrane, while it reveals the whole time course of the *change* in the eardrum's vibration. What is the reason for this phenomenon? Does this phenomenon occur for all kinds of models? Where does the ascent of $Q(\Delta t)$ come from?

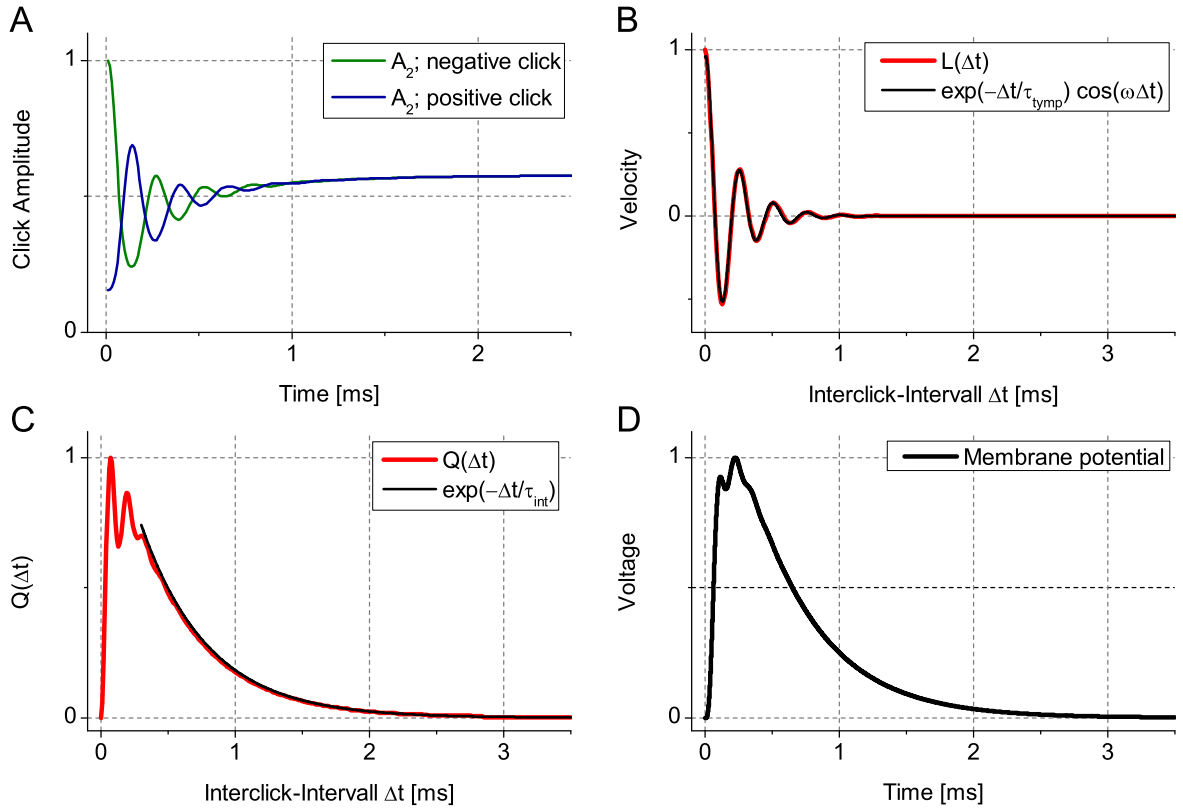

Figure 3.1: SIMULATION OF ISO-RESPONSE-SETS. For each iso-response-set two clicks were presented, separated by a time interval, Δt. The amplitude of the first click, A_1, was held constant throughout the experiment. The amplitude of the second click was then adjusted to yield the desired spike probability. To be able to unravel the two linear filters of the transduction chain, two different stimulus patterns had to be measured. Here, the second click was either presented in the same ('*positive*', A_2) direction or in the opposite ('*negative*', $\tilde{A}_2$) direction as the first click.
(A) Time course of the click-amplitudes A_2 and $\tilde{A}_2$, resulting in the same spike probability and, thus, corresponding to the same output value of the effective stimulus intensity J. Both amplitudes were normalized to to $\tilde{A}_2$ (B) Time course of the *change* of the eardrum vibration, $L(\Delta t)$ (red line), calculated from the measured values A_2 and $\tilde{A}_2$ (Eq. 1.10). The results are compared to a damped harmonic oscillator (black line, Eq. 3.4) with fundamental frequency $f = 4\,\text{kHz}$ and decay time constant $\tau_{tymp} = 200\,\mu\text{s}$ of the modeled filter function $l(\Delta t)$. (C) Time course of the electrical integration process, $Q(\Delta t)$ (red line, Eq. 1.11). The measured data are compared to an exponential decay function with the time constant $\tau_{int} = 500\,\mu\text{s}$ of the modelled filter $q(\Delta t)$ (Eq. 3.6). (D) The model's voltage curve was calculated by Eq. (3.6) without white noise in response to a single click. Figures B-D show normalized values.

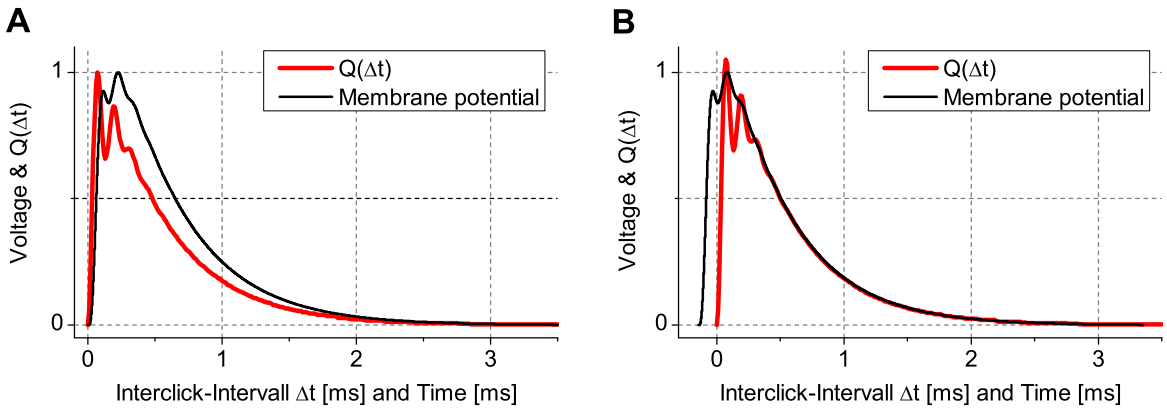

Figure 3.2: COMPARISON OF THE MODEL'S VOLTAGE RESPONSE AND FILTER $Q(\Delta t)$. (A) The voltage curve in response to a click and $Q(\Delta t)$ don't match right away. (B) The voltage curve of the model has to be shifted to match the filter function, indicating that the method reveals a part of the electrical integration process only. Clearly visible are the early oscillations of the eardrum, which appearance in $Q(\Delta t)$ is a characteristic trait of the indirect iso-response method.

3.2.1 Where does the Ascent of $Q(\Delta t)$ come from?

A look into the mathematical foundations of the general cascade model, as derived in Gollisch and Herz (2005), reveals that several assumptions were necessary to yield the relationships between $l(\tau)$ and $L(\Delta t)$ as well as between $Q(\Delta t)$ and $q(\tau)$. For understanding the properties of $Q(\Delta t)$ we here review this calculation.

The connection of the generalized cascade model and its click version (Section 1.4.4) is derived as follows. The response of the receptor neuron $r(t)$ is given by

$$r(t) = \tilde{g}\,(J(t)) \tag{3.9}$$

$$\text{with} \quad J(t) = \int_0^\infty d\tau'\, q(\tau') \cdot \left[\int_0^\infty d\tau\, l(\tau) \cdot A(t-\tau-\tau') \right]^2 . \tag{3.10}$$

The following causality conditions are assumed to apply for the filter functions $l(\tau)$ and $q(\tau)$:

$$l(\tau) = q(\tau) = 0 \text{ for } \tau < 0 \tag{3.11}$$

The function $r(t)$ can be interpreted as the instantaneous firing rate and, therefore,

$$p = \int_T^{T+w} r(t) \cdot dt \tag{3.12}$$

is the probability of finding a spike in the time window w beginning at time T. With Equations (3.2), (3.3) and (3.8) the relationsships $(\tau_1 > 0, \tau_2 > 0)$

$$l(\tau_1+\tau_2) = l(\tau_1) \cdot \tilde{l}(\tau_2) + l(\tau_2) \cdot \tilde{l}(\tau_1) \quad \text{and} \tag{3.13}$$

$$q(\tau_1+\tau_2) = q(\tau_1) \cdot q(\tau_2) \tag{3.14}$$

hold.

In order to relate the generalized model (Eq. 3.10) to the click model (Eq. 1.5), we use a pair of clicks (modeled as Dirac delta functions) with amplitudes A_1 and A_2 as inputs to the general model. For clicks at times $t_1 = 0$ and $t_2 = \Delta t > 0$ the input reads

$$A(t) = A_1 \cdot \delta(t) + A_2 \cdot \delta(t - \Delta t). \tag{3.15}$$

To continue with the calculation, some basic assumptions have to be made. We can assume that the effective stimuli intensity $J(t)$ has a rather stereotypic, sharply peaked form and that it will be adjusted to yield the same maximum J. We assume that the spike probability p will be dominated by the maximum J. Simulations show that the maximum J, and thus the relevant instant of spike initiation, is obtained at the same times T after the second click, for different click combinations. Thus, spikes are initiated at $t = \Delta t\ + T$. Inserting $A(t)$ Eq. (3.15) to Eq. (3.10) we obtain for J at time $t = \Delta t + T$

$$J = J(\Delta t + T) = \int_0^\infty d\tau \left[A_1 \cdot l(\Delta t + T - \tau) + A_2 \cdot l(T - \tau)\right]^2 \cdot q(\tau). \tag{3.16}$$

The right-hand side of the term decomposes into

$$\begin{aligned} J = {} & A_1^2 \cdot q(\Delta t) \cdot \int_0^{\Delta t} d\tau\ [l(\tau)]^2 \cdot q(T - \tau) \\ & + [A_1 \cdot \tilde{l}(\Delta t) + A_2]^2 \cdot \int_0^T d\tau\ [l(\tau)]^2 \cdot q(T - \tau) \\ & + A_1^2 \cdot l^2(\Delta t) \cdot \int_0^T d\tau\ [\tilde{l}(\tau)]^2 \cdot q(T - \tau) \\ & + 2 \cdot A_1 \cdot l(\Delta t) \cdot [A_1 \cdot \tilde{l}(\Delta t) + A_2] \cdot \int_0^T d\tau\ \tilde{l}(\tau) \cdot l(\tau) \cdot q(T - \tau). \end{aligned} \tag{3.17}$$

The last term can be neglected as it will be small compared to the other integrals. Here, we want to construct a form of J that is similar to Eq. (1.7) of the click-model in the introduction. To obtain a comparable form, the following definitions are used:

$$k = \int_0^T d\tau\ [l(\tau)]^2 \cdot q(T - \tau), \tag{3.18}$$

$$\zeta = \frac{1}{k} \cdot \int_0^T d\tau\ [\tilde{l}(\tau)]^2 \cdot q(T - \tau), \tag{3.19}$$

$$\gamma(\Delta t) = \frac{1}{k} \cdot \int_0^{\Delta t} d\tau\ [l(\tau)]^2 \cdot q(T - \tau). \tag{3.20}$$

Eq. (3.17) can then be written as

$$J = A_1^2 \cdot q(\Delta t) \cdot \gamma(\Delta t) \cdot k + [A_1 \cdot \tilde{l}(\Delta t) + A_2]^2 \cdot k + A_1^2 \cdot [l(\Delta t)]^2 \cdot \zeta \cdot k \tag{3.21}$$

$$\Longleftrightarrow J = A_1^2 \cdot \{q(\Delta t) \cdot \gamma(\Delta t) + [l(\Delta t)]^2 \cdot \zeta\} \cdot k + A_1 \cdot \tilde{l}(\Delta t) \cdot k + A_2^2 \cdot k. \tag{3.22}$$

The constant factor k can be absorbed into the relation between J and p. By comparison with the Equation from the click-model,

$$J = A_1^2 \cdot Q(\Delta t)\ +\ [A_1 \cdot L(\Delta t)\ +\ A_2]^2 \tag{3.23}$$

we find the relationships

$$L(\Delta t) = \tilde{l}(\Delta t) \tag{3.24}$$

$$Q(\Delta t) = q(\Delta t) \cdot \gamma(\Delta t) + [l(\Delta t)]^2 \cdot \zeta. \tag{3.25}$$

$L(\Delta t)$ therefore corresponds to a phase-shifted version of the filter $l(\Delta t)$ and can thus be interpreted as the velocity of the tympanic vibration.

First, $Q(\Delta t)$ is related to $q(\Delta t)$, but not identical to it. The identity of $Q(\Delta t)$ is more complicated and explains the occurence of an initial rise of this filter function. The correction factor ζ is a constant near unity. The factor $[l(\Delta t)]^2$ is a squared damped sine function (Eq. 3.13), with $l(\Delta t) = 0$ for $\Delta t = 0$. It has a strong oscillatory influence on $Q(\Delta t)$ for early Δt, but converges quickly to zero for larger Δt, since $\tau_{Tymp} \ll \tau_{int}$. For this reason the term $[l(\Delta t)]^2 \cdot \zeta$ is negligible for $\Delta t \gg \tau_{Tymp}$. The term $\gamma(\Delta t)$, on the other hand, is zero for $\Delta t = 0$ and approaches unity for larger Δt due to the fast decay of $[l(\Delta t)]^2$, because then the integral in Eq. (3.20) will become equal to k in Eq. (3.18). Note, that the $l^2(\Delta t)$ terms decay with $\tau_{tymp}/2$ due to the square function that separates the two linear filter functions:

$$\left(e^{\frac{-t}{\tau_{tymp}}}\right)^2 = e^{-2\frac{t}{\tau_{tymp}}} = e^{-\frac{t}{\tau_{tymp}/2}} \tag{3.26}$$

The mathematical details of the relationship of the click-version model and the generalized cascade model explain the initial shape of $Q(\Delta t)$ for small interclick intervals, Δt. The calculations demonstrate that the initial oscillations are a characteristic trait of this indirect approach, but don't correspond to biophysical processes.

3.2.2 Why doesn't $Q(\Delta t)$ reveal the whole time course?

Our simulations demonstrated that the time course of $L(\Delta t)$ captures the whole oscillation of the eardrum. This result is very comprehensible. Any second click impulse has to be charged against the oscillation caused by the first click impulse and, thus, *must* be found in the iso-response sets from the first moment of the triggered oscillation.

Another intuition can be given for the finding that only a part of the electrical integration is captured by the IRS. Any spike is obviously evoked by the maximum of the impulse response (Fig. 4.2), which is denoted by J. Roughly speaking, both clicks cause individual potentials that superimpose, when the interclick interval is small enough. The maximum of the potential evoked by the second click can by no means occur earlier than the maximum of the potential of the first click. Hence, any inter-click interval, Δt, shifts the maximum of the second potential away from the maximum of first potential. It now happens that the voltage curve evoked by the first click descents in time and any second click has to compensate this descent to yield the same spike probability. Thus, it occurs to be plausible that the IRS captures only those parts of the electrical integration after the maximum of the first evoked potential.

The calculation in Section 3.2.1 provides the means to understand this phenomenon mathematically. In order to yield Eq. (3.16), we first assumed that the maximum J of $J(t)$ is the relevant parameter for the tuning of spike probability. Second, we assumed that the maximum J always occurs at time $\Delta t + T$ and, therefore, $J \equiv J(\Delta t + T)$. For interclick intervals $\Delta t = 0$, we coherently get $J \equiv J(T)$, which is thus the smallest time of the effective stimulus intensity we can measure by iso-response sets. In our simulation in Section 3.1, $J(t)$ is identical to $V_m(t)$ and we can thus write $J \equiv V_m(T)$.

3.2.3 The Impulse Response of the Signal Transduction Chain

In order to understand the relationships between $Q(\Delta t)$ and the voltage trace of the model in response to a short click, we calculate the impulse response of the model. The air pressure wave for a single short click is given by

$$A(t) = A_1 \cdot \delta(t) \tag{3.27}$$

To calculate the impulse response of the signal transduction chain we insert Eq. (3.27) into Eq. (3.10) and get

$$J(t) = \int_0^\infty d\tau'\, q(\tau') \cdot \Big[\int_0^\infty d\tau\, l(\tau) \cdot A_1 \cdot \delta(t-\tau-\tau') \Big]^2 \tag{3.28}$$

$$\iff J(t) = A_1^2 \cdot \int_0^\infty d\tau\, q(\tau)\, [l(t-\tau)]^2 \tag{3.29}$$

Figure (3.2) suggests that the impulse response needs to be shifted to the left to be comparable wit $Q(\Delta t)$. Following the arguments from Section 3.2.2 we assume that this shift equals the time T of the peak. The shifted impulse response then reads

$$J(t+T) = A_1^2 \cdot \int_0^t d\tau\, q(\tau)\, [l(t+T-\tau)]^2 \tag{3.30}$$

This is exactly Eq. (3.16) with $A_2 = 0$ and we can read of the solution from Eq. (3.22) to be

$$J(t+T) = A_1^2 \cdot \{q(t) \cdot \gamma(t) + \tilde{l}^2(t) + l^2(t) \cdot \zeta\} \cdot k + A_1 \cdot \tilde{l}(\Delta t) \cdot k \tag{3.31}$$

$$= A_1^2 \cdot Q(\Delta t) + A_1 \cdot \tilde{l}(\Delta t) \cdot k, \tag{3.32}$$

where the dependency on T is contained in $\gamma(t)$ (Eq. 3.20) and ζ (Eq. 3.19).

To be in agreement with our observations the impulse response (Eq. 3.32) and $Q(\Delta t)$ (Eq. 3.25) should be equal for sufficiently large interclick intervals, Δt. In this case, all terms containing $l(\tau)$ converge to zero and Eq. (3.32) reduces to

$$J(t+T) = A_1^2 \cdot Q(\Delta t) \cdot k. \tag{3.33}$$

However, for small interclick intervals Eq. (3.25) and Eq. (3.32) differ significantly, which is in agreement with our observations in Figure (3.2B).

3.2.4 A Non-Oscillatory Eardrum

To strengthen our reasoning of Section (3.2.1) about the influence of the $l(\Delta t)$ terms on $Q(\Delta t)$, we investigate a model without oscillatory components (Fig. 3.3). We substitute $l(\tau)$ (Eq. 3.2) with

$$l(\tau) = e^{-\frac{\tau}{\tau_{tymp}}}, \tag{3.34}$$

which is modeled by

$$\tau_{tymp}\, \frac{d}{dt}\, x(t) = -x(t) + s(t) \tag{3.35}$$

All other parameters are similar to the original model in Section 3.1. In the previous chapter we demonstrated that $Q(\Delta t)$ reveals the part $J(t)$ after the time T, only. As this is a general characteristic of the iso-response method, this characteristic applies here, too, and we can expect $Q(\Delta t)$ to begin with the maximum of $J(t)$. However, similar to section 3.2.1, we have to consider the influence of the term $\gamma(\Delta t)$.

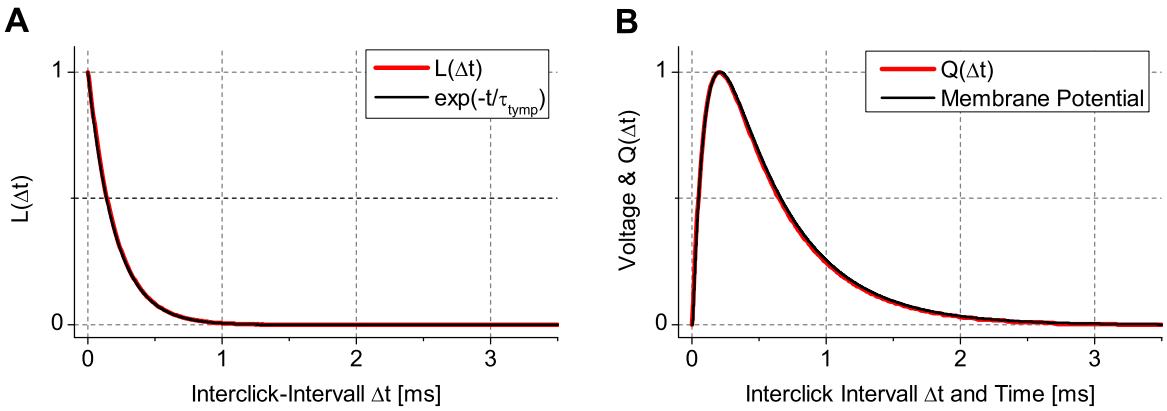

Figure 3.3: MODEL WITH A NON-OSCILLATORY EARDRUM. (A) Time course of the change of the eardrum vibration, $L(\Delta t)$ (red line), calculated from the measured values A_2 and $\tilde{A}_2$ (Eq. 1.10). The measured data are compared to an exponential decay function with the time constant $\tau_{tymp} = 200\,\mu s$ of the modelled filter $l(\Delta t)$ (Eq. 3.35). (B) Time course of the electrical integration process, $Q(\Delta t)$ (red line, Eq. 1.11). The measured data are compared to the time course of the convolution (2.4) with $\tau_1 = 0.5 \cdot \tau_{tymp} = 100\,\mu s$ and $\tau_2 = \tau_{int} = 500\,\mu s$ of the modelled filter $q(\Delta t)$. Filter $Q(\Delta t)$ matches perfectly with the voltage curve and unravels the whole time course of the electrical integration.

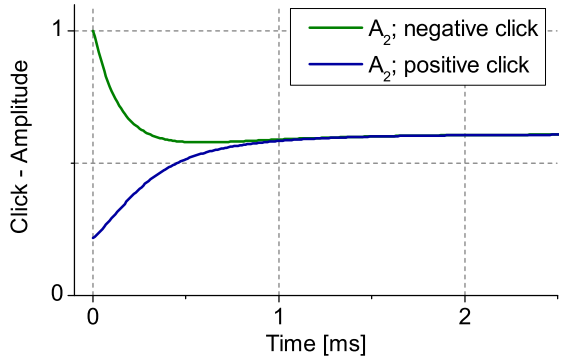

Figure 3.4: TIME COURSE OF THE CLICK-AMPLITUDES A_2 AND $\tilde{A}_2$ The later part of the time course of A_2 is clearly governed by the time constant $\tau_{int} = 500\,\mu s$ of $q(\Delta t)$. The time course of $\tilde{A}_2$ comprises additional information about the time course of $l(\tau)$, (Fig. 3.3A).

Theoretical Considerations

To find the relationships between $Q(\Delta t)$ and $q(\tau)$ we perform a calculation analogous to that in Section (3.2.1). Starting with Eq. (3.16), we get

$$\begin{aligned} J &= \int_0^{\Delta t} d\tau\, A_1^2 \cdot \big[l(\tau)\big]^2 \cdot q(\Delta t) \cdot q(T-\tau) \\ &\quad + \int_0^{T} d\tau \big[A_1 \cdot l(\Delta t) \cdot l(\tau) + A_2 \cdot l(\tau)\big]^2 \cdot q(T-\tau) \end{aligned} \tag{3.36}$$

$$\begin{aligned} J &= A_1^2 \cdot q(\Delta t) \cdot \int_0^{\Delta t} d\tau\, \big[l(\tau)\big]^2 \cdot q(T-\tau) \\ &\quad + \left(\big[A_1 \cdot l(\Delta t)\big]^2 + A_2^2 + 2A_1A_2 \cdot l(\Delta t) \right) \cdot \int_0^{T} d\tau\, \big[l(\tau)\big]^2 \cdot q(T-\tau) \end{aligned} \tag{3.37}$$

Using the following definitions

$$k = \int_0^{T} d\tau\, \big[l(\tau)\big]^2 \cdot q(T-\tau) \tag{3.38}$$

$$\gamma(\Delta t) = \int_0^{\Delta t} d\tau\, \big[l(\tau)\big]^2 \cdot q(T-\tau). \tag{3.39}$$

we get

$$J = A_1^2 \cdot q(\Delta t) \cdot k \cdot \gamma(\Delta t) + \big(A_1 \cdot l(\Delta t) + A_2\big)^2 \cdot k \tag{3.40}$$

In comparison with Eq. (3.23) for the click-model, we find

$$L(\Delta t) = l(\Delta t) \tag{3.41}$$

$$Q(\Delta t) = q(\Delta t) \cdot \gamma(\Delta t) \tag{3.42}$$

This is an exact solution and no approximations by neglecting terms like in the original calculation had to be made. In Eq. (3.42) we again find the factor $\gamma(\Delta t)$, while the term $[l(\Delta t)]^2 \cdot \zeta$ we obtained in Equation (3.25) has vanished. The term $\gamma(\Delta t)$ approaches unity due to the fast convergence of $[l(\Delta t)]^2 = \exp[-\Delta t/(\tau/2)]$ to zero.

In this model we find $Q(\Delta t)$ to be identical to the impulse response of the transduction chain. We read

$$Q(\Delta t) = q(\Delta t) \cdot \gamma(\Delta t) \tag{3.43}$$

$$= \int_0^{\Delta t} d\tau\, [l(\tau)]^2 \cdot q(T-\tau) \cdot q(\Delta t) \tag{3.44}$$

$$= \int_0^{\Delta t} d\tau\, [l(\tau)]^2 \cdot q(T+\Delta t-\tau) \tag{3.45}$$

$$= ([l(\tau)]^2 * q)(T+\Delta t), \tag{3.46}$$

which is the convolution of the functional filters of the model. In Section 3.2.2 we argued that $Q(\Delta t)$ captures $J(T+\Delta t)$ only and, still, here we find the whole time course of J revealed. This is possible due to the correction factor $\gamma(\Delta t)$, which, in this model, happens to be identical with the convolution of the functional filters.

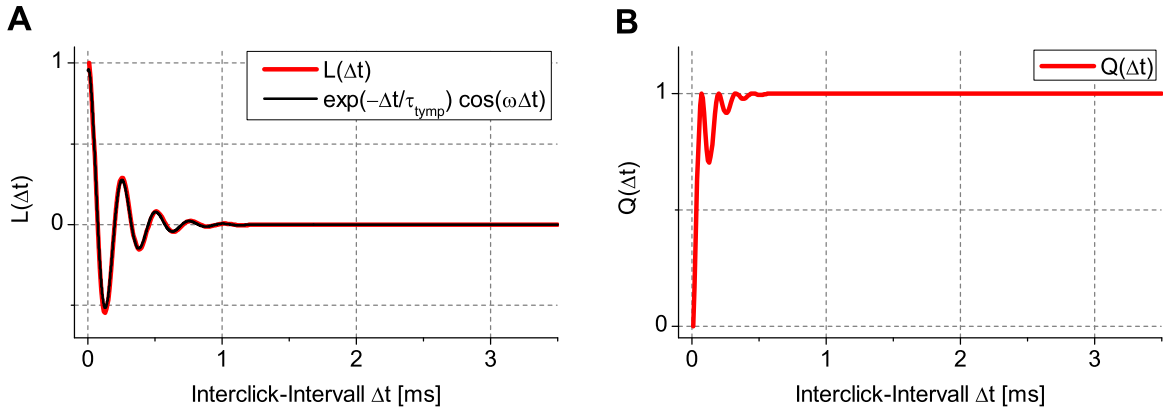

Figure 3.5: ISO-RESPONSE-SETS FOR THE 'INTEGRAL'-MODEL. (A) Time course of the *change* of the eardrum vibration, $L(\Delta t)$ (red line), calculated from the measured values A_2 and $\tilde{A}_2$ (Eq. 1.10). The results are compared to a damped harmonic oscillator (black line, Eq. 3.4) with fundamental frequency $f = 4$ kHz and decay time constant $\tau_{tymp} = 200\,\mu$s of the modeled filter function $l(\Delta t)$. (B) Time course of the electrical integration process, $Q(\Delta t)$ (red line, Eq. 1.11). In this case, the iso-response-set doesn't reveal any information about the electrical integration. This approach reveals the oscillatory effects of the iso-response method for small Δt, which are found in $Q(\Delta t)$ of the other model-versions,too.

Both linear filter functions, $l(\tau)$ and $q(\tau)$, have the same form as the convolutions we investigated in Chapter 2 and we thus find

$$Q(\Delta t) = \frac{\frac{1}{2}\cdot\tau_{tymp}\cdot\tau_{int}}{\frac{1}{2}\cdot\tau_{tymp}-\tau_{int}}\left[e^{-\frac{2\Delta t}{\tau_{tymp}}} - e^{-\frac{\Delta t}{\tau_{int}}}\right] \tag{3.47}$$

Thus, the time course of $Q(\Delta t)$ in Figure (3.3) is identical to that in Figure (2.1A).

3.2.5 Illumination of the Artificial Elements in $Q(\Delta t)$

It is possible to display the combined effects of the terms $\gamma(\Delta t)$ and $[l(\Delta t)]^2\cdot\zeta$ in Equation (3.25). The model we used for reproducing the iso-response sets of Gollisch and Herz still used a probabilistic output function to calculate the desired spike probability p. Instead, we now use an deterministic approach and calculate the integral over the whole time course $J(t)$ to compute the 'spike probability' p:

$$p = J = \int_0^\infty J(t)\,dt = constant \tag{3.48}$$

Due to the integral function, both click amplitudes A_1 and A_2 fully contribute to J. As both clicks are added independently of the electrical integration, represented by filter $q(\Delta t)$, this implies $q(\Delta t) = 1$. Considering this, Equation (3.25) decomposes to

$$Q(\Delta t) = \gamma(\Delta t) + [l(\Delta t)]^2\cdot\zeta. \tag{3.49}$$

Therefore, $Q(\Delta t)$ describes the effects of the terms $\gamma(\Delta t)$ and $[l(\Delta t)]^2\cdot\zeta$ only (Fig. 3.5). Comparison with Figure 3.2 explains the initial rise of $Q(\Delta t)$ from zero and the differences to the time course of the voltage curve. Note, that both $\gamma(\Delta t)$ and ζ contain the term $q(\Delta t) = 1$ and, hence, are not identical to Eq. (3.19) and Eq. (3.20). However, the difference is small as the dynamics of $q(\Delta t)$ are slower than that of $l(\Delta t)$ and the influence of $l(\Delta t)$ on $Q(\Delta t)$ becomes apparent. In Section 3.2.1 we proposed that the decay time of $l(\Delta t)$ would be halved due to the squaring. Here, we find these predictions confirmed by comparison of the time course of $L(\Delta t)$ and $Q(\Delta t)$ in Figures (3.5A) and (3.5B), respectively.

3.3 Replacing the Quadratic Nonlinearity with the Absolute Value Function

Apparently, the quadratic nonlinearity makes it possible to separate the filter functions $l(\tau)$ and $q(\tau)$. However, a complete retrieval of $q(\Delta t)$ is not possible. Here we investigate how the first nonlinearity influences this result by using an absolute value function instead of the quadratic nonlinearity. This would still yield the important rectification characteristic. At the same time the influence of $l(\tau)$ in time is extended, as the shortening influence of the squaring is absent (see Section 3.2.1). The resulting signal transduction cascade has the form

$$s(t) \xrightarrow{l(\tau)} \xrightarrow{|\cdot|} \xrightarrow{q(\tau)} J(t) \xrightarrow{g(\cdot)} p. \tag{3.50}$$

Due to the substitution of the static quadratic nonlinearity by absolute values, we require a different equation for computing $L(\Delta t)$ and $Q(\Delta t)$ from the click experiments. We derive the required equations by a similar calculation to that in Section 1.4.4. In our simulations, we tune each pair of stimuli (A_1, A_2) and $(A_1, \tilde{A}_2)$ to yield the same spike probability J, so that $J(A_1, A_2) = J(A_1, \tilde{A}_2)$. The effective stimuli intensity for each pair of clicks is given by

$$J = A_1 \cdot Q(\Delta t) + |A_1 \cdot L(\Delta t) + A_2| \tag{3.51}$$

$$J = A_1 \cdot Q(\Delta t) + |A_1 \cdot L(\Delta t) - \tilde{A}_2| \tag{3.52}$$

Setting those equations equal, we get

$$|A_1 \cdot L(\Delta t) + A_2| = |A_1 \cdot L(\Delta t) - \tilde{A}_2| \tag{3.53}$$

No matter, if $L(\Delta t)$ is positive or negative, A_2 is tuned in such a way that the term on the left-hand side is always positive. We thus read

$$A_1 \cdot L(\Delta t) + A_2 = |A_1 \cdot L(\Delta t) - \tilde{A}_2| \tag{3.54}$$

The solution $A_2 = -\tilde{A}_2$, for the case that the right-hand side is positive, doesn't correspond to a physical situation, as A_2 and $\tilde{A}_2$ denote absolute values. The only remaining case is that $-\tilde{A}_2$ is tuned in such a way that the term on the right-hand side is always negative. We then find

$$L(\Delta t) = \frac{\tilde{A}_2 - A_2}{2A_1} \tag{3.55}$$

and via substitution into Eq. (3.51)

$$Q(\Delta t) = -\frac{\tilde{A}_2 + A_2}{2A_1}. \tag{3.56}$$

The difference to the solution of the original model (Eqn. 1.11) is the missing square in the solution for $Q(\Delta t)$. Here, it seems that $Q(\Delta t)$ captures the whole time course of the electrical integration (Fig. 3.6). Unfortunately, the explicit calculation of the relationships between $Q(\Delta t)$ and $q(\tau)$ is not possible due to the absolute value function.

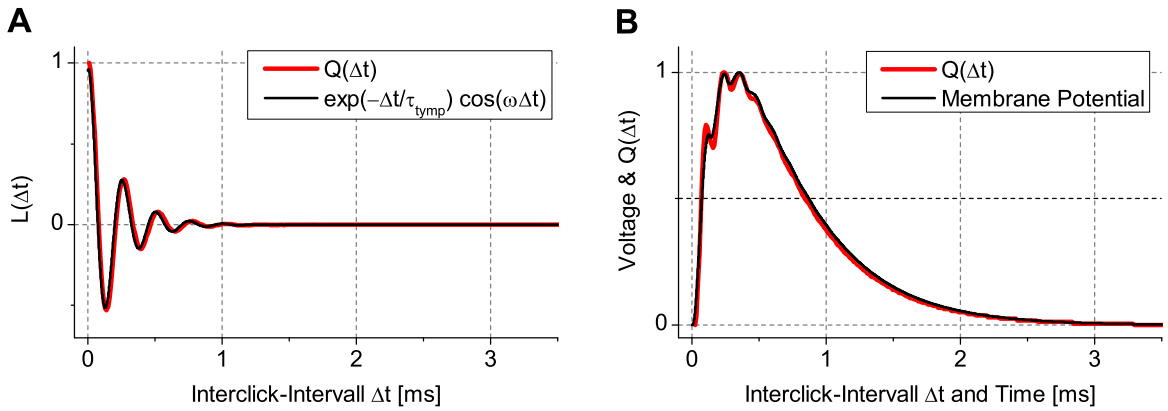

Figure 3.6: ISO-RESPONSE-SETS FOR THE ABSOLUTE-VALUE-MODEL. (A) Time course of the *change* of the eardrum vibration, $L(\Delta t)$ (red line), calculated from the measured values A_2 and $\tilde{A}_2$ (Eq. 1.10). The results are compared to a damped harmonic oscillator (black line, Eq. 3.4) with fundamental frequency $f = 4\,\mathrm{kHz}$ and decay time constant $\tau_{tymp} = 200\,\mu\mathrm{s}$ of the modeled filter function $l(\Delta t)$. (B) Comparison of the electrical integration process, $Q(\Delta t)$ (red line), and of the models's impulse response. Both curves match well and Filter $Q(\Delta t)$ seems to contain information about the whole time course of the electrical integration.

3.4 Do we find Properties of the Spike-Generator in $Q(\Delta t)$?

The last nonlinearity in the generalized cascade model of locust signal transduction describes the transformation of a receptor potential to a firing rate or spike probability, respectively. This step certainly involves the spike generator. Here, we discover a difficulty in defining what we mean exactly with the term 'spike-generator'. In the study of Gollisch et al. the process of spike-generation was functionally described by the filter function $\tilde{g}(\cdot)$, which translates the effective stimulus intensity J into a spike response of the receptor neuron. It was assumed to be a static, monotonously rising function with sigmoidal shape (Gollisch and Herz (2005)). This assumption is true for our initial simulation of iso-response sets in Section (3.1).

There, the electrical integration of accumulating charge at the cell membrane was modelled by the filter function $q(\tau)$. The convolution of the input signal $s(t)$ with the first three filter functions yields the effective stimulus intensity J. Finally, J is transformed to a spike probability by means of an integral over the complementary error function (Eq. 3.7), which possesses the claimed monotonous sigmoidal shape. Here, the processes of electrical integration and spike generation are modeled separately and can clearly be distinguished.

But of course, a patch of passive dendritic membrane, as it is modeled by $q(\tau)$ integrates accumulating charges differently (meaning linear) than a spike-generator with its voltage-dependent ion-channels (meaning nonlinear). A simple and commonly used standard model is the leaky integrate-and-fire model, which exhibits the same characteristics as the approach we used before in Section (3.1). It would be straight forward to simulate a signal transduction chain with a full conduction based model of a spike-generator as output function. The signal transduction chain we use here has the functional form

$$s(t) \xrightarrow{l(\tau)} \xrightarrow{|\cdot|} \xrightarrow{q(\tau)} \xrightarrow{j(\cdot)} p \tag{3.57}$$

where $j(\cdot)$ stands for the spike-generator model and the effective stimulus intensity J is embedded in $j(\cdot)$.

The Hodgkin-Huxley model has been derived from the giant axon of the squid and exhibits oscillations in the range of 20 Hz (Hodgkin and Huxley, 1952a,b,c,d). The Traub-Miles model builds up on the Hodgkin-Huxley model, but parameters were adapted to model the response

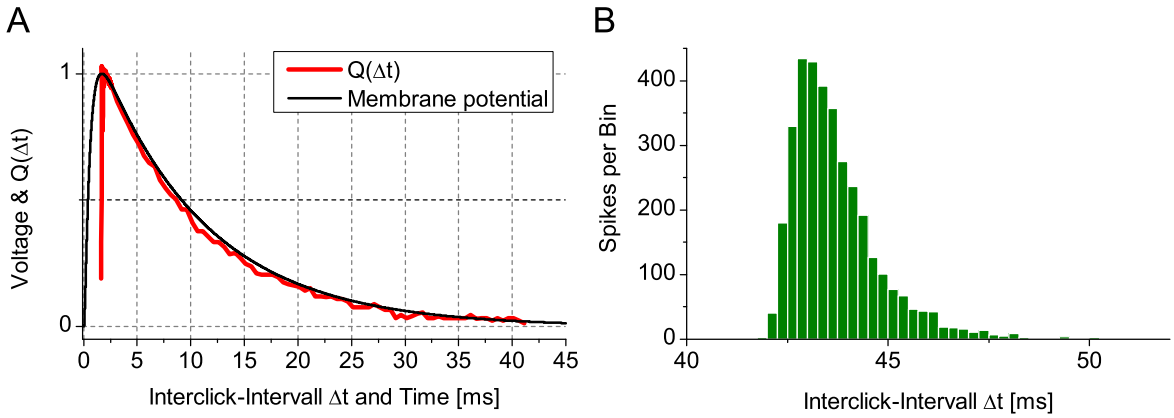

Figure 3.7: MEASUREMENTS OF ISO-RESPONSE-SETS IN THE 'TRAUB-AND-MILES'-MODEL. (A) Time course of the electrical integration process, $Q(\Delta t)$ (red line, Eq. 1.11). The measured data are compared to the model's impulse response. $Q(\Delta t)$ and the impulse response match well and indicate that the dynamics of this model are captured by the iso-response sets. (B) Histogram of the spike time variability at $\Delta t = 40$ ms. Simulations of this model span 60 ms. Thus, we here show that our simulation captured all evoked spikes at the longest simulated interclick interval.

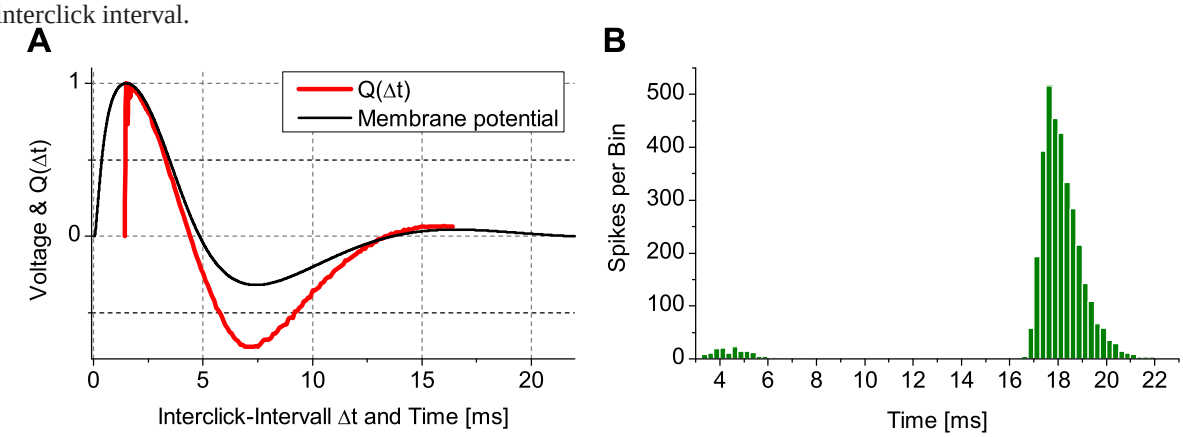

Figure 3.8: MEASUREMENTS OF ISO-RESPONSE-SETS IN THE 'HODGKIN-HUXLEY'-MODEL. (A) Time course of the electrical integration process, $Q(\Delta t)$ (red line, Eq. 1.11). $Q(\Delta t)$ reveals a part of the voltage curve only. The Hodgkin-Huxley-model shows slow oscillations which are not captured exactly by the method. (B) Histogram of the spike time variability at $\Delta t = 15$ ms. Simulations of this model span 60 ms. Thus, we here show that our simulation captured all evoked spikes at the longest simulated interclick interval. Some spikes were evoked much earlier by the first click.

behaviour of the pyramidal neurons in CA3 (Traub et al., 1991). Due to these differences, the Traub-Miles model shows much slower dynamics than the Hodgkin-Huxley model. These two models behave in a complex way and combine the processes of electrical integration and spike-generation in a single framework. It is not possible to explicitly distinguish the nonlinear function that transforms the effective stimulus intensity J into the spike-probability p from the preceding integration. Details of the models are left to the appendix.

Similar to Section 3.1, two iso-response sets are performed with a stimulus $s(t)$, consisting of two short clicks (width 10 µs). The first click amplitude is held positive throughout the simulations, while the second click was either positive for the first IRS or negative for the second IRS. The stimulus $s(t)$ is convolved with the filter function $l(\tau)$, the result is squared and convolved with filter function $q(\tau)$, yielding the membrane potential $V_m(t)$. The input $I(t)$ for the spike-generator model is then given by

$$I(t) = S \cdot V_m(t) + D \cdot \xi \tag{3.58}$$

with the input-scaling factor S, noise ξ and noise-strength factor D.

Both models possess much slower dynamics than the locust auditory system. For that reason we have to simulate a much longer time than we did in previous simulations. If the simulation time is too small to capture all spikes for larger Δt, the spike probability p will be underestimated and compensated by higher tuned amplitudes. This would result in a systematic tuning error, while Δt gets larger. Both models exhibit a relative broad spike-jitter. To make sure no spikes were lost we present histograms of the spiketimes together with our results (Figures 3.7B and 3.8B).

The input threshold of the Traub-Miles model is close to $I = 0$ and thus spikes are easily evoked. This results in spontaneous activity even with low noise that distorts our results. For that reason we added a negative baseline input ($I_{base} = -1\,\mu\text{A/cm}^2$) to Eq. (3.58) to eliminate spontaneous activity.

The dynamical properties of both models change strongly in proximity to the threshold. Therefore, we chose the first click's amplitude in such a way that it results in a typical and uniform shaped impulse response as it can be observed for click-amplitudes far away from the threshold (Fig. 3.8A, black curve). For details see appendix.

Traub-Miles Results are shown in Figure (3.7). The iso-response sets yield a very good approximation of the time course of the electrical integration of the spike generator. But as might have been expected, all integrative parts of the spike-generator are captured by $Q(\Delta t)$, additionally to oscillatory parts of $l(\tau)$ for early Δt. As in Section (3.1), only the part of the time course of the membrane potential beyond the peak is revealed. Oscillatory components of the tympanum are found in the very early phase of $Q(\Delta t)$.

Hodgkin-Huxley Here, too, integrational parts of the spike-generator are captured by the IRS. In comparison with the time course of the membrane potential, we find a very biased $Q(\Delta t)$ (Fig. 3.8A). The initial and the last part of the time course seem to fit well with the membrane potential, but the negative phase in between is too large. These results suggest that either the spike-generator influences the extraction of $Q(\Delta t)$ in an unexpected way or something else must have changed.

The filter $L(\Delta t)$ was reliably measured for both models. Also, both simulations show, that the IRS captures all integrational parts of the spike-generator, beginning with the time T of the effective spike initiation.

3.4.1 Why can't we reproduce the $V_m(t)$ of the Hodgkin-Huxley-Model?

Phenomenons close to the Threshold Since the first click brings the Hodgkin-Huxley model already close to the threshold, it might be possible that the iso-response method scans for properties of the spike-generator close to the threshold. This phenomenon might lead to the particular shape of $Q(\Delta t)$ we yield for this simulation. To investigate this possibility, we explored how the impulse response of the Hodgkin-Huxley model changes when it's driven close to the threshold by single clicks without evoking an action potential. Examples for this are shown in Figure (3.9). In comparison with the time course in Figure (3.8A) the negative phase of the impulse response gets larger the closer the system gets to the threshold. The response shown in Figure (3.9A) seems to match $Q(\Delta t)$ much better than Figure (3.8A), but the negative phase of impulse response still doesn't get as large as $Q(\Delta t)$. As the system gets even closer to the threshold, the slope of the descent changes dramatically, too, and the final shape of the impulse response becomes very unalike to that of $Q(\Delta t)$ (Figure 3.9B). We conclude, that the shape of the measured $Q(\Delta t)$ is unlikely to be based on such phenomena close to threshold as we investigated them here.

Another approach to analyze the particular behaviour of the Hodgkin-Huxley model in proximity to the threshold is to add a positive baseline-input to the model. The constant input pushes the model towards the threshold and thus changes the steady-state parameters of the model, which results in a different response behaviour. We explored the behaviour in response of the model to a single click for different baseline-inputs. Results are shown in Figure (3.10) for two different values of baseline-input. The negative phase gets larger with higher baseline input and fits the initial and negative part of $Q(\Delta t)$ well. However, as a side effect of baseline-input the oscillatory frequency of the Hodgkin-Huxley model is increased, while the damping of the oscillation is decreased, leading to a large positive oscillation. Therefore, we conclude again that this approach doesn't lead to a satisfying explanation of the shape of $Q(\Delta t)$.

Matching $Q(\Delta t)$ with the Tail of the Voltage Trace Instead of matching the initial phase of $Q(\Delta t)$ to the voltage trace, we scaled $Q(\Delta t)$ to match the tail of the impulse response of the model to single click (Fig. 3.11A). The offset of $Q(\Delta t)$ is equal to the time until the peak of the impulse response is reached. The curves fit well after about 3 ms in respect to the time scale of $Q(\Delta t)$. This time span corresponds well with the time course of the impulse response $V_m(t)$ in the simulations of Section 3.1 (Fig. 3.1D). Hence, it might be that the difference between the impulse response and $Q(\Delta t)$ of the Hodgkin-Huxley model is due to the influence of the filter function $q(\tau)$. Due to the complexity of the Hodgkin-Huxley model ...

Simulating a cascade model without $q(\tau)$ results in a $Q(\Delta t)$ (Fig. 3.11B) that differs only minimal to the $Q(\Delta t)$ obtained from the model including the $q(\tau)$ filter. This was expected since $q(\tau)$ operates on much faster time scales than the Hodgkin-Huxley model. The Hodgkin-Huxley model has not a fixed filter function, but it rather heavily depends on input current and voltage. Therefore, we are not able to establish a good match between $Q(\Delta t)$ and various impulse responses. The IRS, thus, reveals the properties of a very particular dynamic regime of the spike generator only.

Chapter Summary

In this Chapter, we used a simple structured model to reproduce iso-response sets performed by Gollisch and Herz (2005) by means of numerical simulations. We extracted the filters $L(\Delta t)$

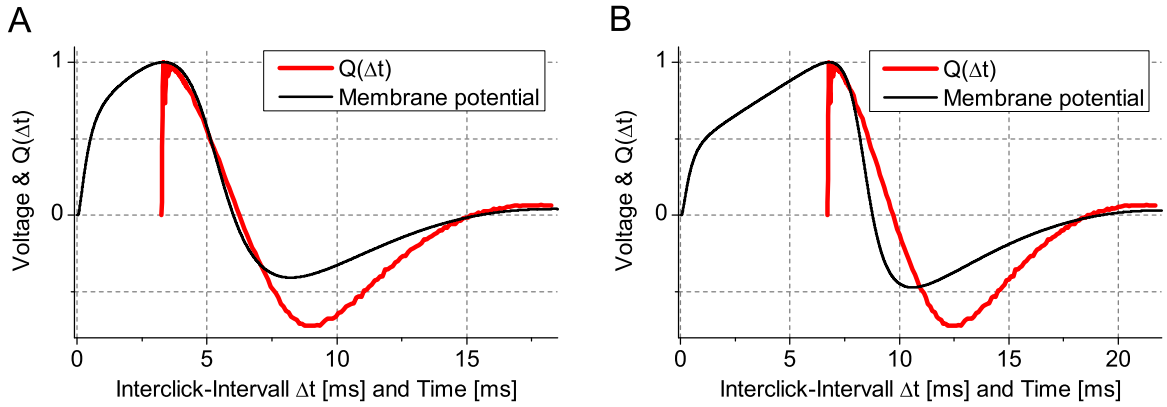

Figure 3.9: HODGKIN-HUXLEY: BEHAVIOUR CLOSE TO THE THRESHOLD . Here we investigate the impulse response of a Hodgkin-Huxley-model which is driven close to the threshold ($A = 6150.3$) by a click impulse. We compare the impulse response to the measured $Q(\Delta t)$. (A) Amplitude $A = 6100$. (B) Amplitude $A = 6150$. Although the amplitude of the oscillation increases the closer the model gets to the threshold, the mismatch of the impulse response and the results of the iso-response-method can't be explained by this approach.

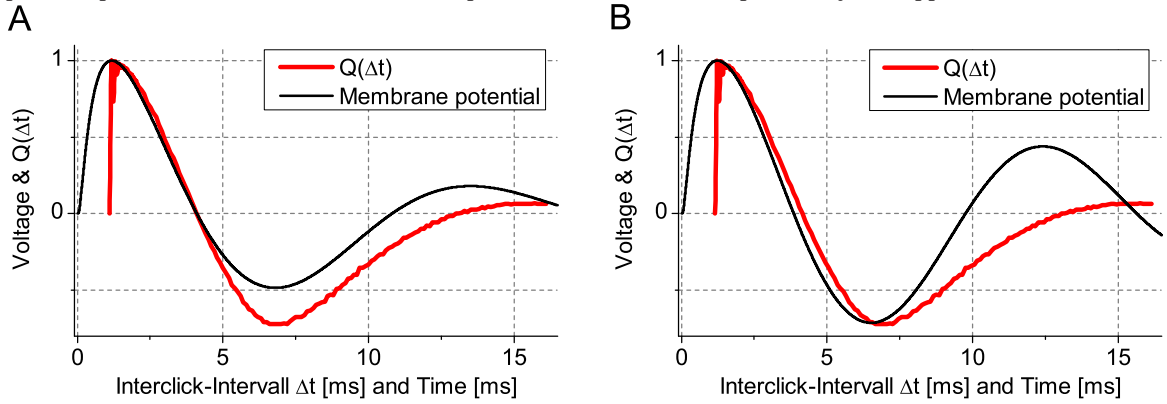

Figure 3.10: HODGKIN-HUXLEY: BEHAVIOUR WITH BASELINE-INPUTS. In addition to the clicks, the model is driven by a baseline-input $I_0 = 5$ (A) and $I_0 = 6$ (B), which shifts the impulse response of the model closer towards the threshold and thus changes it's behaviour. The click-amplitudes are relatively low, so that the model doesn't show close-to-threshold behaviour, as it does in figure 3.9. The higher the baseline-input the more increases the oscillatory frequency of the Hodgkin-Huxley model. We don't find such behaviour in our iso-response-measurements. The mismatch of the impulse response and the results of the iso-response-method can't be explained by this approach.

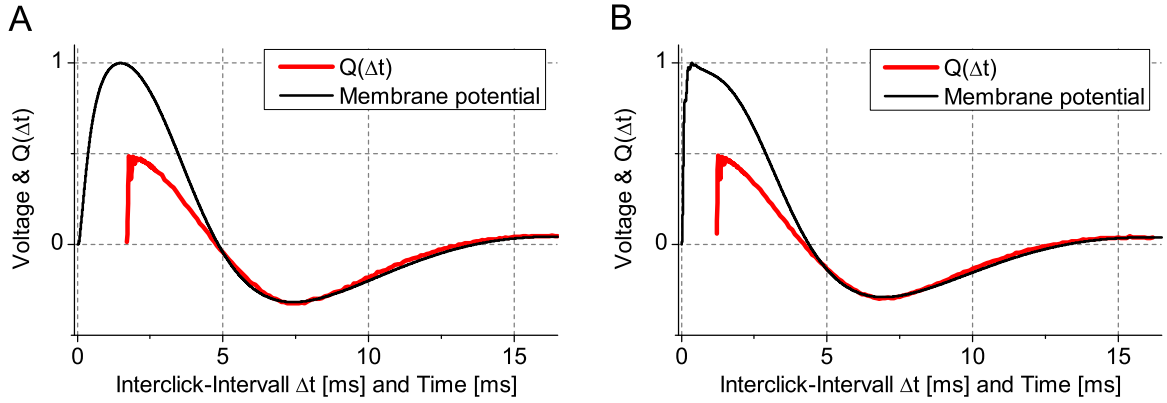

Figure 3.11: $Q(\Delta t)$ FITTET TO THE TAIL OF THE IMPULSE RESPONSE. We fitted $Q(\Delta t)$ to the tail of the impulse response of a single click. Two different models are shown. (A) A Hodgin-Huxley model receives its input by filter $q(\Delta t)$. (B) A Hodgin-Huxley model without the filter $q(\Delta t)$. The curves match well for large interclick intervals, i.e. $\Delta t > 5$s. The initial region of $Q(\Delta t)$ doesn't match well with both models. These findings for both models demonstrate that the initial mismatch of $Q(\Delta t)$ is not due to the influence of the filter function $q(\Delta t)$.

and $Q(\Delta t)$ and demonstrated that essential parameters of the model can be reliably extracted by the IRS. By comparison of the $Q(\Delta t)$ and the impulse response of the model we learned that $Q(\Delta t)$ reveals only a part of the effective stimulus intensity $J(t)$. We demonstrated that all integrative properties of the spike generator are captured by IRS and, thus, IRS measure the temporal integration characteristics of the site of the spike initiation. We also demonstrated that dynamics of the spike-generator can distort the initial phase of $Q(\Delta t)$ and that this distortion is independent of the linear filters $l(\Delta t)$ and $q(\Delta t)$.

CHAPTER 4

ISO-RESPONSE SETS IN AMPLITUDE SPACE OF TWO SHORT CLICKS

Gollisch and Herz (2005) used IRS to analyze amplitude space and thus to determine what stimulus parameters govern locust auditory signal processing on different time scales. Input stimuli consisted of two positive click-impulses with a width of 20 µs each, which were separated by an interclick-interval Δt. Multiple measurements were performed for different amplitude-ratios A_1/A_2 and tuned for each amplitude-ratio to yield the same spike probability of $p = 0.7$. Figure (1.6) shows iso-response sets in amplitude space as they have been measured by Gollisch and Herz (2005). These measurements as interpreted demonstrated that on different time scales, different stimulus parameters govern signal processing: the amplitude A of a sound stimulus for short times and its energy A^2 for long times. Here we compare iso-response sets derived from simulations of different cascade models in respect to this interpretation.

4.1 Simulation of the original cascade model

Similar to the experiments of Gollisch et al., the simulated iso-response sets (Fig. 4.1), feature several particular shapes that can easily be distinguished and are interpreted to reflect different modes of stimulus integration. For short interclick-intervals ($\Delta t \leq 40\,\mu s$), straight lines indicate almost linear summation of the click amplitudes A_1 and A_2.

Dominant oscillations of the eardrum govern the shape of the IRS curves for intermediate interclick-intervals, up to approximately $\Delta t \approx 500\,\mu s$, where the oscillations caused by $l(\Delta t)$ dye out (Fig. 4.1; see also Section 3.2.5 and Fig. 3.5;). At this range of intervals, the IRS shapes rapidly change their form with the interclick-interval Δt. The IRS display almost symmetric curves and asymmetric bulbed curves (shown for $\Delta t = 120\,\mu s$ for comparison with Fig. 1.6). The influence of the eardrum (and thus of filter function $l(\Delta t)$) is vanishes for larger interclick intervals, $\Delta t > 500\,\mu s$, and the shape of the IRS curves are governed by the process of electrical integration, $q(\Delta t)$. We find asymmetric curves for values of Δt of 500 µs and 750 µs (Fig. 3.5). As larger Δt grows, the curves resemble more closely the shape of a square ($\Delta t = 2.5\,ms$, Fig. 3.5).

Why are the iso-response sets for a larger Δt slightly asymmetric curves instead of ellipses? And why do the iso-response sets approach the shape of squares for a large Δt? In order to understand this phenomenon we recapitulate how the model responds to a single pair of clicks (Fig 4.2). The first click initiates the vibration of the eardrum, the deflection of the eardrum is

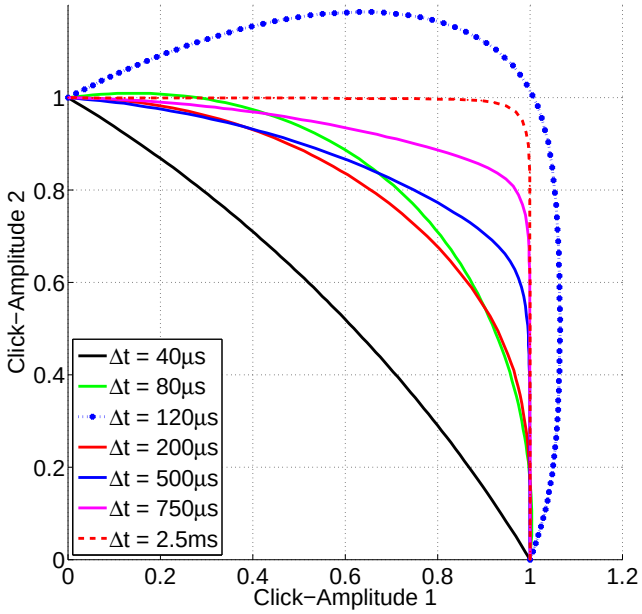

Figure 4.1: REPRODUCTION OF ISO-RESPONSE SETS IN AMPLITUDE SPACE FOR FIXED TIME INTERVALS Δt. Each iso-response measurements was performed with double-click stimuli for a fixed interclick time interval Δt each. Multiple ratios of the click amplitudes A_1/A_2 were tuned to yield the desired spike probabilty p. As in the experiments published by Gollisch and Herz (2005), several prominent shapes of iso-response-sets can be distinguished: straight lines, circles, ellipses and, additionally, squares. The shapes are interpreted to reflect different modes of stimulus integration in the signal transduction cascade of the locust.

squared and serves as input for the passive membrane. In response to the input by the eardrum vibration an electrical potential over the membrane builds up (Fig. 3.1C). In case of a larger interclick interval, e.g. $\Delta t = 750\,\mu$s, the influence of the vibration of the eardrum due to the first click will have almost died out. The second click will initiate the eardrum vibration anew, this evoking an independent electrical potential. Because the second click was initiated before the potential evoked by the first click had converged to steady-state, both *electrical potentials* are added linearly (Fig. 4.2). Roughly speaking, in this scenario the potential evoked by second click has a 'headstart' because it builds up on the electrical potential evoked by the first click, which leads to the asymmetric shape of the IRS. The shape of the IRS will thus be dependent on the value of $Q(\Delta t)$ at a particular interclick interval Δt.

A different situation is found for very large interclick interval, e.g. $\Delta t = 2.5\,$ms, where the membrane potential evoked by the first click has already converged to zero. Both clicks are then independent in respect to electrical integration as the second click's potential doesn't build up on the potential of the first click. For large and small amplitude-ratios A_1/A_2 only one of the clicks will contribute to the spike probability p, which results in a square-like shape of the iso-response sets. Figure (4.1) shows such a square for $\Delta t = 2.5\,$ms. For amplitude-ratios close to unity the IRS displays a circle-like shape. The radius of this circle is dependent on the noise added to the system, which can easily be shown in simulations.

This phenomenon can be understood by means of Equation 4.1 for the effective stimulus strength J of the click-model,

$$J = A_1^2 \cdot Q(\Delta t) \; + \; [A_1 \cdot L(\Delta t) \; + \; A_2]^2 \,. \tag{4.1}$$

In order to explain the observations of straight lines, asymmetric curves and the square-like

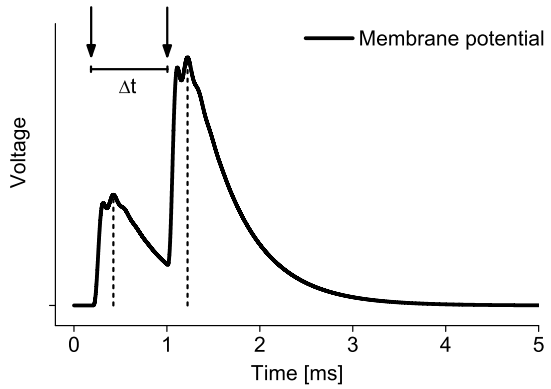

Figure 4.2: SUCCESSIVE CLICKS. The membrane potential in response to a sequence of two short clicks (indicated by arrows), which are separated by the interclick interval, Δt. The potential evoked by the second click, A_2, builds up on the the potential evoked by the first click, A_1. The dashed lines indicate the peaks of evoked membrane potentials. This example corresponds to the situation governed by Eq. (4.3) and helps to understand, why the IRS for $\Delta t > 500\,\mu$s exhibit asymmetric ellipses.

shape, we distinguish three cases.

1. $\Delta t = 0$. Neither the eardrum vibration, nor the electrical integration are initiated. Thus, $Q(\Delta t)$ is zero and $L(\Delta t)$ equals unity, as we found in Section 3.2, Eq. 3.24 and 3.25. Therefore, Eq. (4.1) reduces to
$$J = [A_1 + A_2]^2\,, \tag{4.2}$$
which is a linear summation of the click amplitudes A_1 and A_2, resulting in a straight line in amplitude-space.

2. At all zero crossings of $L(\Delta t)$ and at interclick intervals of $\Delta t > 500\,\mu$s, when the eardrum oscillation died out, we find $L(\Delta t) = 0$ and Eq. (4.1) reads
$$J = A_1^2 \cdot Q(\Delta t) + A_2^2. \tag{4.3}$$
This equation describes the ellipses we find in Figure (4.1).

3. For interclick intervals $\Delta t > 2.5\,$ms both $L(\Delta t)$ and $Q(\Delta t)$. Equation (4.1) remains
$$J = A_2^2. \tag{4.4}$$
When the click amplitude A_2 is sufficiently larger (the specific ratio between A_1 and A_2 is dependent of the noise of the system) than the click amplitude A_1, almost all spikes are evoked due to A_2. In this case, the click amplitudes A_1 and A_2 will be tuned until A_2 is large enough to cause the desired spike probability, resulting in a horizontal curve in the amplitude space in Figure (4.1), for $\Delta t = 2.5\,$ms. The reciprocal case occurs, when the click amplitude A_1 is sufficiently larger than the click amplitude A_2. Then all spikes are evoked due to A_1 and, in the experiment, A_1 and A_2 are tuned until A_1 is large enough to yield the desired spike probability. The result is a vertical line in Figure (4.1), for $\Delta t = 2.5\,$ms.

The results of our simulations match very well with the results obtained by Gollisch and Herz (2005) in Figure (1.6). IRS for short interclick intervals, $\Delta t = 40\,\mu$s, exhibit straight lines

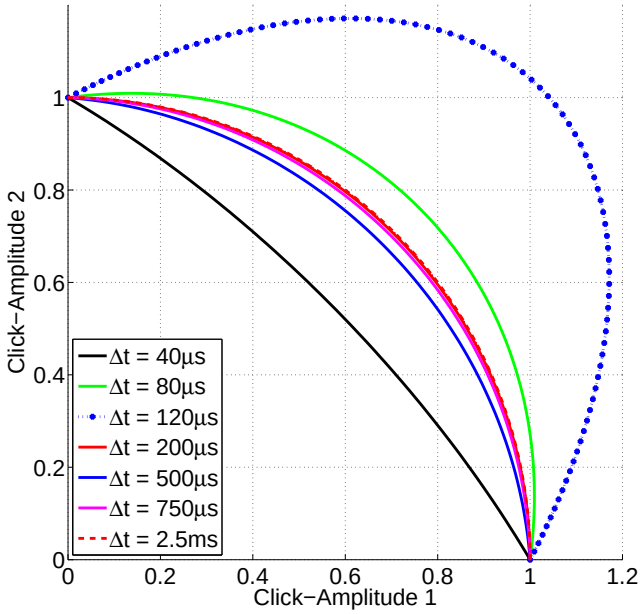

Figure 4.3: OSCILLATIONS IN AMPLITUDE SPACE DUE TO $l(\tau)$. Here, the output function was an integral of $J(t)$, as described before in Section 3.2.5. For large Δt IRS are mere circles, reflecting the quadratic summation of the amplitudes. For small Δt the strong oscillations of the eardrum causes the IRS to form ellipses, which change form rapidly with Δt.

and bulb-shaped curves for $\Delta t = 120\,\mu s$. We also find slightly asymmetric ellipses for $\Delta t = 500\,\mu s$ and $750\,\mu s$.

We don't find symmetric ellipses for these interclick intervals. We propose that the differences between the experimental data and an asymmetric shaped ellipses for these interclick intervals is covered by the noise in the experimental data. This interpretation is supported by much higher standard deviations of the data in Figure (1.6A) compared to Figures (1.6B and C). The square-like shaped IRS are not measured in the study of Gollisch and Herz due to too small interclick intervals, Δt.

4.2 Simulations of Alternative Cascade Models

Oscillatory Components By integrating over $J(t)$ as output function g we are able to directly show the oscillatory influence of $l(\tau)$ on the IRS in amplitude space (Fig. 4.3). Here, the iso-response sets exhibit symmetric ellipses for large interclick intervals, i.e. $\Delta t > 500\,\mu s$, while the IRS curves for smaller Δt are symmetric curves that vary strongly with Δt. The latter phenomenon reflects the rapid oscillations of the eardrum.

Due to the integral function, both click amplitudes A_1 and A_2 fully contribute to J in regard to their evoked electrical potential. Therefore, no contribution of either click is 'forgotten' and no 'independent' clicks exist. Since the first click amplitude always fully contributes to J, this implies no dependence of $q(\Delta t)$ and therefore $Q(\Delta t) = 1$. Applying this relation to Equation (4.3), we get for large Δt when $L(\Delta t) = 0$

$$J = A_1^2 + A_2^2, \tag{4.5}$$

which explains the symmetric ellipses, we observe for large interclick intervals, $\Delta t > 500\,\mu s$.

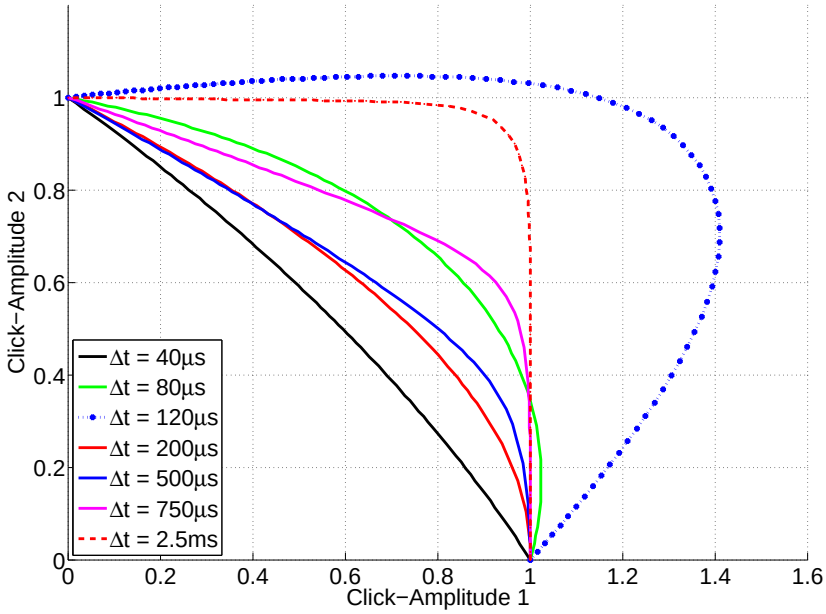

Figure 4.4: LNLN-CASCADE WITH ABSOLUTE VALUES. Main differences to the reproduction-model are a stronger asymmetry of the ellipses for large Δt and a slower 'growth' to the square-like shape of independent clicks. The similarity of these result to the reproduction model indicate that IRS in amplitude-space are inappropriate to unravel the nature of the second nonlinearity without profound knowledge of the signal transduction cascade.

We can't comprehend the symmetry of the IRS for small Δt by means of equations.

Replacing the Quadratic Nonlinearity with the Absolute Value function Here, we use the cascade model introduced in Section 3.3. The cascade model comprises the absolute value function instead of the quadratic nonlinearity. The iso-response sets for this model (Fig. 4.4) exhibit shapes very similar to the original model (Fig. 4.1). Main differences are a much more pronounced asymmetry of the ellipses for small Δt and a slower 'growth' of the asymmetric ellipses for large Δt to the square-like shape of independent clicks. As explained in Section (3.2.1), the quadratic nonlinearity causes τ_{tymp} effectively to be halved. The absence of this effect in this model leads to the prolonged influence of $l(\Delta t)$ and the greater asymmetry of the ellipses for small interclick intervals.

Hodgkin-Huxley The cascade model with a Hodgkin-Huxley model as output function exhibits particularly interesting oscillations in the 20 Hz range (Fig. 3.8). The iso-response sets for this model show highly symmetrical shapes for small Δt. Here, we find IRS that exhibit straight lines, ellipses, circles and squares, as we found them in original model (Fig. 4.1). Additionally, we find nose-like shaped IRS that reflect the oscillations of the Hodgkin-Huxley-model at large Δt ($>$ 3ms). When the voltage response of the model enters a negative phase, the second click has to compensate for the negative offset of the voltage curve. This results in the nose-like shapes of IRS for Δt corresponding to a negative phase of the voltage curve.

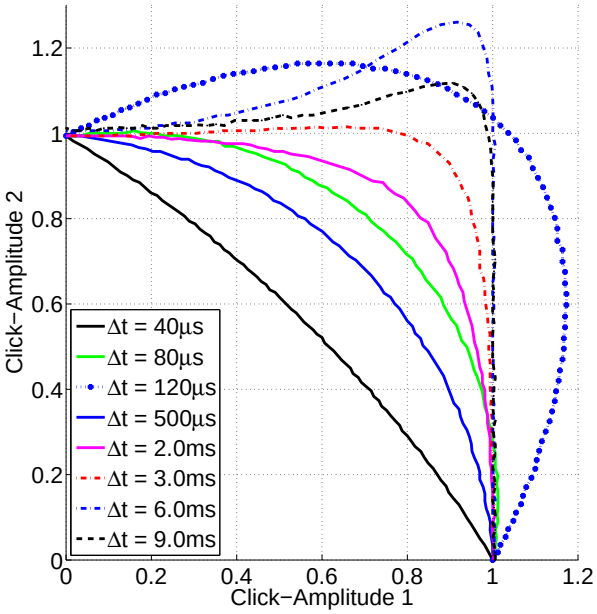

Figure 4.5: ISO-RESPONSE SETS WITH A HODGKIN-HUXLEY MODEL. For short Δt we find linear summation (straight lines), for medium-ranged Δt the oscillatory influence of the eardrum causes rapidly changing ellipses. For longer Δt, IRS continue to grow to a square-like shapes, similar to those observed in the simulation of the original model (Fig. 4.1). The shapes of these IRS are approximately symmetrical. The oscillatory behaviour of the Hodgkin-Huxley model results in nose-like shaped IRS for the negative phases of the oscillation of the membrane potential for large Δt.

Chapter Summary

We have shown that the IRS in amplitude space of Gollisch and Herz (2005) can be reproduced with a simple structured model. Furthermore, we have shown that asymmetric instead of symmetric ellipses are the prominent shape of iso-response sets in amplitude space for large interclick intervals, Δt, when the filter function $l(\Delta t)$ almost converged to zero. For very large Δt iso-response sets converge to a square-like shape with a rounded edge, which specific radius depends on the noise of the system. We have shown, that the bulb-shaped curves for small interclick intervals are a characteristic trait of the eardrum oscillation only.Our results suggest that the elliptical shape for iso-response sets for large Δt, as proposed by Gollisch and Herz (2005), is not a strong argument for a quadratic nonlinearity between the filter functions $l(\tau)$ and $q(\tau)$, since this is heavily distorted by $L(\Delta t)$ and $Q(\Delta t)$ and dependend on $g(\cdot)$. However, this quadratic nonlinearity has been independently measured by the analysis of the spectral integration of pure sine tones (Gollisch et al. (2002)).

CHAPTER 5

SEPARATION OF FUNCTIONAL SUBMODULES BY MEANS OF NOISE

The iso-response method offers the means to analyze the locust auditory signal transduction chain, as it is characteristic of this method to enable the unraveling of the linear filter functions of the LNLN-cascade. The identification of these linear filter functions is possible only because they are separated by a single nonlinearity. The terminal nonlinearity remains without effect for this analysis due to the very definition of iso-response (see Section 1.4.3). The processes described by the linear filter functions are might be divided in further functional submodules that reflect the underlying biophysical processes in even greater detail. These functional submodules can't be unraveled by the iso-response method, as they are not separated by a significant nonlinear process. For that reason the submodules act as a single filter function, similar to the convolutions of exponential functions we investigated in Chapter 2.

Yet it might be that a scenario exists, where some submodules are captured better by this method than others. As a possibility, this scenario could apply, when two functional modules are separated by a high level of noise. Here, we analyze this specific scenario in order to understand whether some functional components of the linear filter functions are not or only weakly captured by IRS.

For this purpose, we composed a signal transduction chain (a LNLN-cascade) that features a second linearity, which is composed of two linear submodules (a LNLLN-cascade so to speak, Eq. 5.1). These submodules are a sequence of two exponential decay functions that the IRS typically captures as a single linear filter. The signal transduction chain we use here has the form

$$s(t) \xrightarrow{l(\tau)} \xrightarrow{[\cdot]^2} \xrightarrow{q(\tau)} \xrightarrow{w(\tau)} J(t) \xrightarrow{g(\cdot)} r(t), \tag{5.1}$$

where the filter functions are given by

$$l(\tau) = sin(2\pi f \cdot t) \cdot e^{-\frac{t}{\tau_{Tymp}}}, \tag{5.2}$$

$$q(\tau) = e^{-\frac{t}{\tau_q}}, \tag{5.3}$$

$$w(\tau) = e^{-\frac{t}{\tau_w}}. \tag{5.4}$$

Although a significant amount of noise could be added to the signal at different positions of the transduction chain, we are, in this case, only interested on the effects of noise added to the output of $q(\tau)$. This output is then convolved with $w(\tau)$, yielding the effective stimulus intensity

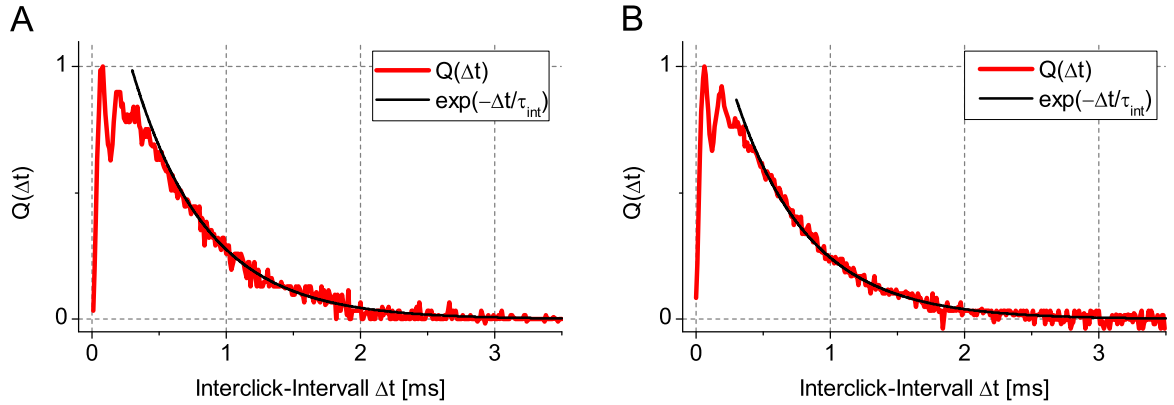

Figure 5.1: SEPARATING EFFECTS OF NOISE. We modeled an LNLLN-cascade and investigated if it is possible to separate the second, $q(\tau)$, and third linearity, $w(\tau)$, with a high-level of noise in between. (A) $\tau_q = 500\,\mu s, \tau_w = 250\,\mu s$. The extracted decay time constant of the tail of $Q(\Delta t)$, $\tau_{int} = 550\,\mu s$, is close to the larger tau_q and indicates that no separation occurs due to high levels of noise. (B) $\tau_q = 250\,\mu s, \tau_w = 500\,\mu s$. The extracted decay time constant of the tail of $Q(\Delta t)$, $\tau_{int} = 550\,\mu s$, is close to the larger tau_w. The results suggest that no separation of filters occurs in this scenario, either.

$J(t)$. In the case that a high level of noise uncouples $q(\tau)$ and $w(\tau)$, the iso-response sets should yield a $Q(\Delta t)$ that mainly reflects the properties of $q(\tau)$ or $w(\tau)$.

Following this paradigm, we model the signal transduction chain by the following steps. The eardrum is simulated by

$$s(t) = \ddot{x}(t) + \frac{2}{\tau_{tymp}}\dot{x}(t) + \omega^2 x(t). \tag{5.5}$$

The output $x(t)$ is squared and serves as input for $q(\tau)$, modeled as

$$\tau_q \frac{d}{dt} V_q(t) = -V_q(t) + x^2(t). \tag{5.6}$$

The output $V_q(t)$ serves as input for $w(\tau)$

$$\tau_w \frac{d}{dt} V_w(t) = -V_w(t) + V_q(t) + D\xi, \tag{5.7}$$

with gaussian white noise ξ and the noise-strength D.

At this point we don't know, if a separation of two filter functions by noise is at all possible. Furthermore, in the case that parameters of one filter are measured better than the other, which of the two filters would it be? To be able to cover both possibilities, we therefore performed two different experiments. In order to distinguish between the characteristics of $q(\tau)$ and $w(\tau)$, we used time constants τ_q and τ_w for the filter functions that differ significantly. We choose a noise-strength factor of $D = 20$, which results in a standard deviation of $\sigma = 20\%$ in respect to the threshold level. In Chapter 2 we demonstrated that in a convolution of two exponential decay filters the filter function with the larger time constant has dominant influence on the decay time of the resulting overall function. In case no decoupling takes place, we will extract a time constant from $Q(\Delta t)$, which is close to the longest time constant of each experimental setup. Otherwise, if we find a decay time constant in $Q(\Delta t)$ that is significantly smaller than the longer time constant of the two filter functions, this would suggest an decoupling of the linear filters.

Experimental Setups

1. $\tau_q = 500\,\mu s$, $\tau_w = 250\,\mu s$. Results are shown in Figure (5.1A). The extracted decay time constant of the tail of $Q(\Delta t)$ is very close to τ_q, which suggests that the filter functions $q(\tau)$ and $w(\tau)$ remain coupled even with high levels of noise added.

2. $\tau_q = 250\,\mu s$, $\tau_w = 500\,\mu s$. Results are shown in Figure (5.1B). Analogous to the first case, the extracted decay time constant of the tail of $Q(\Delta t)$ is very close to τ_w and suggest a coupling of both filter functions, even with high levels of noise added.

Our simulations don't suggest a separation of linear filter due to noise, at least for the scenarios tested. Therefore, it is likely that even in noisy signal transduction chains all sequenced linear filters are captured as a single filter by the iso-response method.

CHAPTER 6

CONCLUSION AND DISCUSSION

The iso-response Sets introduced by Gollisch and Herz (2005) provided a powerful method combining theory and experiments for a functional analysis of the locust auditory signal transduction. This approach yielded detailed novel insights about functional modules of the transduction chain and, by this means, the temporal integration in auditory receptor neurons. The IRS bases upon the analysis of the signal transduction chain as a sequence of functional filters, which transform the input signal $s(t)$ into a lower-dimensional response, e.g. a spike probability.

A remarkable characteristic of the IRS is the reliable detection of the first linearity, $l(\Delta t)$, which remains unmasked by influences of the second linearity, $q(\Delta t)$. In contrast, the estimation of $q(\Delta t)$ from $q(\Delta t)$ is distorted by the first linearity, $l(\Delta t)$, and is, therefore, possible only under certain preconditions. Due to the separating quadratic nonlinearity between $l(\Delta t)$ and $q(\Delta t)$, the decay time constant of $l(\Delta t)$ is halved. However, if the temporal of extension $l^2(\Delta t)$ meets that of $q(\Delta t)$ a reliable extraction of the filter $Q(\Delta t)$ is impossible, as its time course is severely superimposed by $l(\Delta t)$ (Eq. 3.25). Although, this limitation due to $l(\Delta t)$ can't be avoided by this indirect approach, experimental data of Gollisch and Herz suggest that this limitation plays a marginal role *in vivo*, as the eardrum's vibration typically dies out much earlier than the electrical integration ($\tau_{dec}/\tau_{int} \approx 0.2$ to 0.5).

By comparison we found that a shifted impulse response of the signal transduction model matches $Q(\Delta t)$. More generally, we here showed that after the first filter died out the second linearity, $q(\Delta t)$, the impulse response of the signal transduction chain, $V_m(t)$, and the effective stimuli intensity, $J(t)$, are well identified by $Q(\Delta t)$, except for a shift in the time axis by T, which reflects the time after the second click when a spike is evoked. For the original model of Section (3.1), we found the relationships for sufficiently large interclick intervals ($\Delta t \gg \tau_{tymp}$)

$$Q(\Delta t) = q(\Delta t + T) = J(\Delta t + T) = V_m(\Delta t + T). \tag{6.1}$$

The ascent of $q(\Delta t)$ is masked by the influence of $l(\Delta t)$. Unfortunately, information about shorter time constants, which is contained in the ascent of $q(\Delta t)$ (see Chapter 2), is lost by this phenomenon.

In Section (3.2.4) we analyzed a different model, where the whole time course of the effective stimuli strength, $J(t)$, of the auditory transduction chain can be unraveled. The key-feature of this model is a non-oscillatory first linearity with exponential decay characteristics. Due to this characteristics the loss of the initial phase of $J(t)$ until time T is compensated by the correction factor $\gamma(\Delta t)$ which exactly reconstitutes the whole time course of $J(t)$ and, therefore,

of $q(\Delta t)$. This characteristic might be beneficial in future IRS experiments on auditory receptors to analyze the temporal integration of stimuli in greater detail by directly moving the tympanum to abolish the masking effects of the oscillations.

In a neuron spike initiation is more complex than the leaky-integrate-and-fire model we used in our initial analysis. In order to investigate what characteristics of the spike generator are captured by $Q(\Delta t)$, we simulated the full conduction-based models of spike-generators as output function of our signal transduction chain. Our simulations demonstrated that all integrational sub-threshold components of the spike generator are captured, when its dynamics are slower than that of the preceding filters. Also, we found a profound mismatch of the initial phase of $Q(\Delta t)$ and the impulse response that might be attributed to the nonlinear subthreshold properties of the Hodgkin-Huxley model. Another possible reason for the mismatch of impulse response and $Q(\Delta t)$ could lie in the time T, when a spike is evoked. In the original model T is assumed to be a constant. This is not necessarily true for the Hodgkin-Huxley model and could, hence, be the cause of the initial mismatch for small Δt. By our formal analysis of sequenced filters and our elaborations on separation due to noise, we showed that the integrational sub-threshold properties of the spike-generator and other linear filters, e.g. the membrane properties of the dendrite, are unlikely to be separable by the IRS.

$Q(\Delta t)$ is, in any case, the combined second linear filter. If the time constants of individual sequenced linear filters differ greatly, the tail of the overall filter is determined mostly by the longest time constant of the sequenced filters, as shown in Chapter 2.

The application of the iso-response method (Gollisch and Herz, 2005) gave insight into the dependence of successive inputs in respect to time, a characteristic represented by the extracted time constant τ_{int} of the filter $Q(\Delta t)$ (Fig. 1.9). In the study of Gollisch and Herz, τ_{int} was situated between 300-600 µs. How can we put this information into a biophysical context and how far can we stress a reliable interpretation? Here, we will address these questions in two ways. First, we ask if we can put τ_{int} in relationship to the time constant τ_m of the passive membrane (Eq. 1.1) and, if so, what can we learn from that? Second, does the knowledge of τ_{int} give us a hint about the location of the spike generator? In order to approach these questions, it appears to be necessary to begin with a short review of the time constants τ_{int} and τ_m and their relationships.

The membrane time constant, τ_m, is given by $\tau_m = C_m R_m$, where C_m is the specific membrane capacitance (in $\mu F/cm^2$) and R_m the specific membrane resistance (in Ω cm^2), both in respect to a defined patch of passive cell membrane. The membrane time constant describes the time course of the voltage response $V_m(t)$ of a small patch of passive neuronal membrane to a short current step (Eq. 1.1). After one time constant, $V_m(t)$ reaches 63% of the steady state V_∞.

The auditory receptors of locusts are sensory sensilla known as scolopodia (Michelsen, 1971b). These are structural building blocks of the widely distributed chordotonal organs in insects, whose structure has been described in great detail (Smith, 2000; Gray, 1960, Fig. 1.3A). The receptor neuron's dendrite is known to be relatively simple with no branches (Fig. Jacobs et al., 1999, 1.3B). Thus, effects as they can be observed in spatially extended and complex structures of other neurons can be assumed to be small in case of the locust auditory receptors. These considerations suggests, that leak-currents to 'neighboring regions' are small and the actual time course of the membrane potential is governed by the membrane resistance and, thus, by τ_m.

What is τ_{int}? The relationships in Eq. (6.1) provide the basis for identifying τ_{int}. In any case, the time constant τ_{int} describes the *functional characteristics* of the temporal integration

and, thus, of the second linear *functional module* of the auditory transduction chain. The quality of the description is greatly dependent on how well the time course of $Q(\Delta t)$ is described by an exponential decay function of the form

$$q(\tau) = e^{-\frac{\tau}{\tau_{int}}}, \tag{6.2}$$

as it was used to extract τ_{int} in the study of Gollisch and Herz (2005). It might be asked how τ_{int} corresponds to the underlying physical processes of electrical integration. Provided that the second linear filter is indeed well described by Eq. (6.2) and $\tau_{int} = \tau_m$, the answer is given right away. The situation is more complicated, when the second linear filter module of the auditory signal transduction is not ideally described by Eq. (6.2). Such a situation might apply, when the initiation site for action potentials is not in immediate proximity to the site where the receptor potential is evoked. In this case, the receptor potential has to be conveyed there electrotonically. Such a process could be approximated by a sequence of exponential decay functions. In Chapter 2, we learned that such sequences of exponential decay functions with very similar time constants τ_i can distort the overall filter function. In this case, an extracted time constant τ_{int} would overestimate the membrane time constant τ_m . It is not a trivial task to distinguish this scenario from the simpler structured scenario of Equation (6.2) based on experimental data (Fig. 1.9C), since noise makes it impossible to determine the exact shape of $Q(\Delta)$. The determination is hampered further, as $Q(\Delta)$ reveals $J(t+T)$ only and the initial phase of $Q(\Delta)$ is distorted due to the influence of the squared first linearity, $l^2(\tau)$.

Let us now review the literature about the membrane time constant τ_m. Experimentally, τ_m is usually determined by injecting a brief hyperpolarizing current pulse into the soma and recording the voltage response at the same point. Information about τ_m is contained in the decaying phase of V_m and extracted using the so-called 'peeling' method. Here, V_m is plotted on a semilogarithmic scale and the slope of the tail of the decaying phase of V_m is $-1/\tau_m$. Over the last decades, the estimates for τ_m have grown significantly and more recent estimates range from 20 to 50 msec for the major types of central neurons (see, for α-motoneurons: Fleshman et al., 1988; Clements and Redman, 1989; for hippocampal neurons: Brown et al., 1981; for vagal motoneurons: Nitzan et al., 1990; for cerebellar Purkinje cells: Rapp et al., 1994). Estimates have grown even further with tight-seal whole-cell recordings and are approaching 100 msec in slice preparations (Andersen et al., 1990). But exceptions from these high values have been found, too. In slices of the avian cochlear nucleus the time constant has been found to be only 2 msec using whole-cell recording with tight-seal (Reyes et al., 1994).

Estimates are available for *L. migratoria*, too. Hill (1983), deduced an order-of-magnitude approximation from the cut-off frequency in the spectrum of the recorded voltage fluctuations and obtained a value of 10 ms for the time constant of the receptor neuron. But because of the difficulties in obtaining good recordings and the consequently noisy data, there is lots of room for interpretation. Prinz and Ronacher (2002) performed studies, based on the analysis of spike timing in response to sinusoidally modulated stimuli, and yielded estimates near 1 ms for the integration time of the receptor cells. Russel and Sellick (1983) performed an analysis similar to those of Hill and approximated membrane time constants of mammalian hair cells from the cut-off frequencies in the spectrum and yielded approximations between 0.3 and 0.9 ms. These values are remarkable small in the context of time constants of typical neurons.

It has been argued (Gollisch and Herz, 2005) that short time constants are necessary to follow rapid stimulus input. Here, it is important to note that the response time of a neuron or receptor cell, respectively, is not the same as it's membrane time constant. In fact, neurons can respond much quicker to incoming stimuli than membrane time constants suggest, so that these

should more adequately be seen as a measure of how *slow* a neuron or receptor cell, respectively, can respond (Koch et al., 1996).

Here, let us also note, that although the function of hair cells and locust auditory receptor cells is the same, important differences exist. Hair cells are secondary receptor cells and transfer their output via synapses to neurons in the nucleus cochlearis, which have transduction characteristics of their own (e.g. avian chochlear nucleus). Locust auditory receptor cells, on the other hand, are primary receptor cells with their own axons. The lack of a synaptic transmission before long distance transduction to higher neuronal centres complicates the comparibility of both cell types on a non-functional level.

The proximate advantage of a short time constant in a sensory system is the rapid independence of successive inputs on a small time scale and, thus, an enhanced ability to discriminate accurately between these inputs — even under non-optimal input/noise-conditions. It can also be suspected that this implies an enhancement of information rates due to shorter integration times. The downside of a short time constant can be a high leak-current (which results from a small membrane resistance, R_m, which governs the time constant by $\tau_m = R_m C_m$). A small membrane resistance shortens the length-constant λ, which is in case of a passive dendrite governed by

$$\lambda = \sqrt{\frac{R_m}{R_i} \cdot \frac{d}{4}}, \tag{6.3}$$

with the diameter d, the specific membrane resistance R_m and the specific inner resistance, R_i. Here, a small membrane resistance R_m implies a short length constant, λ. Thus, it might be expected that the area of spike initiation (Trigger Zone) has to be in close proximity to the supposed site of transduction-current input, namely the attachment site to the tympanum.

These considerations fit well with observations from Michelsen (1966, 1971b) and Hill (1983). In one type of receptor cell Michelsen (1966) observed two types of spike potentials: large spikes and small spikes, where a large spike was always evoked by a small spike (Figure 6.1A,B). A particular difference between these two types is in the shape. Small spikes never show a repolarizing phase that undershoots the resting potential as large spikes do. Michelsen confirmed these findings for all four groups of receptor cells (1971b) he describes and notes that the small spikes seem most likely to occur in recordings near to the dendrite of the receptor cell. Hill followed up on this observations and termed the small spikes 'apical' spikes, from the inferred site of their generation at the apical membrane of the sensory dendrite, and links their occurrence to the presentation of sound stimuli. He argues that the shape of these apical spikes could be explained with rather 'exotic' ionic conditions where the receptor cell's membrane contacts the receptor lymph. The apical spikes in the locust auditory receptors appear to be conducted electrotonically along the dendrite, which would explain the variation in the recorded amplitudes and broadness of these potentials. The second class of spike potentials, which Hill termed 'basal' spikes, as they are likely to be evoked at the basal dendritic membrane, show characteristics of conventional action potentials in all respects, which seem to be triggered by apical spikes with one to one correspondence. Considering these findings and the short time constant τ_{int} and the implicated short length constant, λ, of the auditory receptors, we may conclude that the occurrence of a short membrane time constant, τ_m, is made possible by the early spike generation at the apical membrane. Figure 6.1C shows the proposed scheme of spike initiation by Hill (1983).

It shall be noted that the occurrence of apical action potentials, close to the site of the evoked receptor potential, is a common phenomenon in many kinds of mechanoreceptor cells

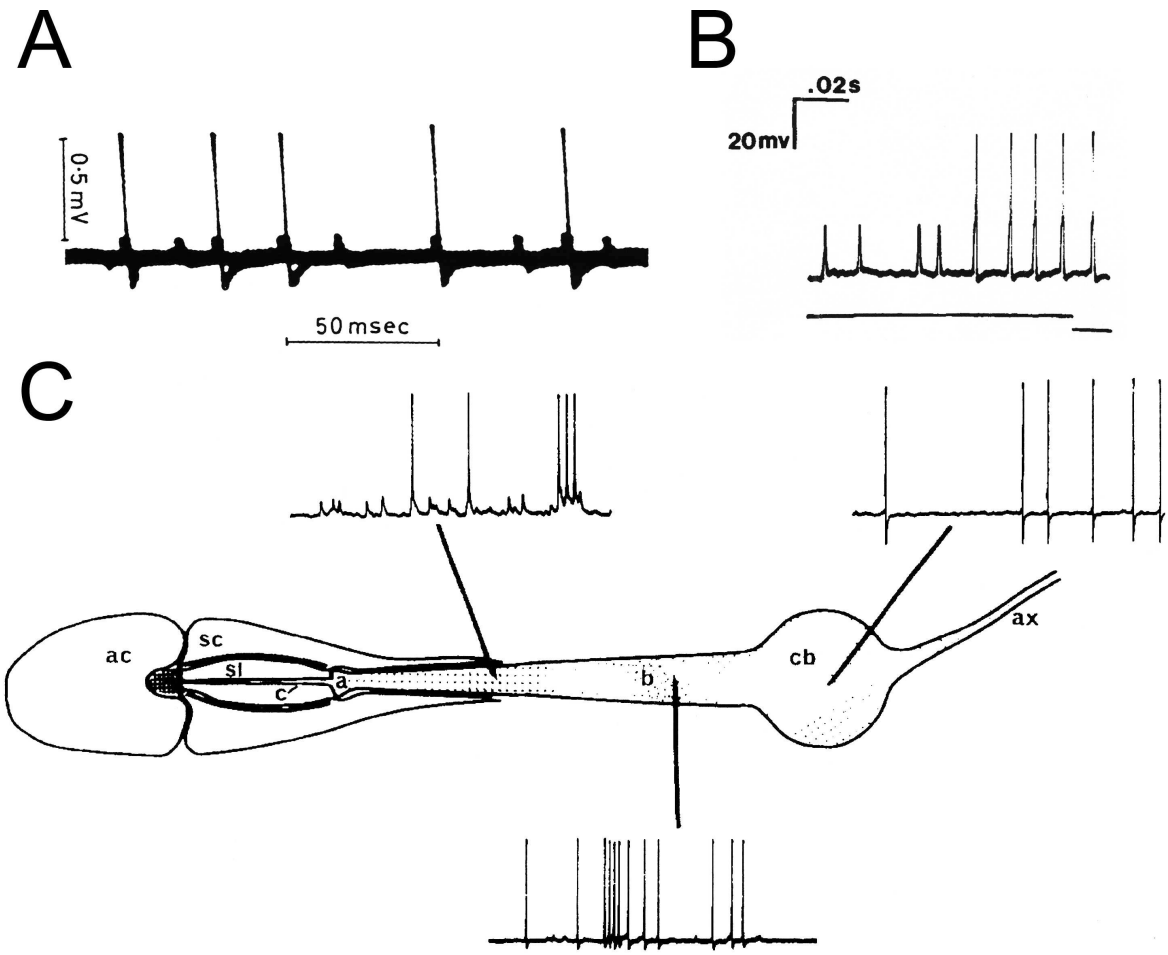

Figure 6.1: RECORDINGS OF APICAL AND BASAL SPIKES AND SITES OF SPIKE INVITATION. (A) First recordings of apical spikes by Michelsen, 1966. Here, apical spikes seem to evoke basal spikes. (B) The response to a sound tone consists initially of small, apical spikes, which begin to trigger basal spikes in the latter part of the response (C) Schematic drawing representing the locust auditory sensillum and showing distinct categories of physiological recordings obtained from receptor cells and the inferred recording sites in each case. The proposition represented in this figure is that transduction occurs at the cilium (c), subthreshold depolarizations and small spikes occur at the apical membrane of the dendrite (a), which is in contact with the receptor lymph contained in the scolopale lumen (sl), which is bounded by the scolopale cell (sc) and attachment cell (ac). Large amplitude basal spikes are initiated in the basal part of the dendrite (b) and are then propagated via the cell body (cb) along the axon (ax) in the tympanal nerve. Figures taken from Michelsen (1971b) (A) and Hill (1983) (B,C).

in mammals. Examples for this are the tactile receptors in the mammalian skin (Pacinian and Meissner's corpuscles), hair follicle receptors, as well as the afferent sensory fibres of the muscle spindle and the Golgi tendon organs (Smith, 2000). All of these examples have in common that the evoked receptor potential spreads electrotonically to a close spike initiating site of the dendrite, far away from the cell body.

The theoretical analysis of the auditory signal transduction raised new and more specific questions about functional aspects of hearing. Direct electrophysiological measurements at the neuron's soma with focus on the location and the characteristics of the spike-generator, as well as on the mechanisms underlying the temporal integration of the auditory receptor neuron would be the next consequential step. The analysis of the locust auditory signal transduction chain is a great example for the benefits of intensive cooperation of theoretical and experimental work.

Appendix

6.1 Hodgkin-Huxley model

The original model of Hodgkin and Huxley (1952d) with the resting potential set to -65mV. The Hodgkin-Huxley model is an example of a class-II neuron.

$$C\dot{V} = -I_{\mathrm{Na}} - I_{\mathrm{K}} - I_{\mathrm{L}} + I$$

Membrane capacitance: C = 1 μF/cm^2.

Sodium current

$$\begin{aligned} I_{\mathrm{Na}} &= \bar{g}_{\mathrm{Na}} m^3 h (V - E_{\mathrm{Na}}) \\ \dot{m} &= \alpha_m(V)(1-m) - \beta_m(V) m \\ \dot{h} &= \alpha_h(V)(1-h) - \beta_h(V) h \end{aligned}$$

$\bar{g}_{\mathrm{Na}} = 120\,\mathrm{mS/cm^2}$, $E_{\mathrm{Na}} = +50\,\mathrm{mV}$,
$\alpha_m(V) = 0.1(V+40)/(1-\exp(-(V+40)/10))$,
$\beta_m(V) = 4\exp(-(V+65)/18)$,
$\alpha_h(V) = 0.07\exp(-(V+65)/20)$,
$\beta_h(V) = 1/(1+\exp(-(V+35)/10))$.

Potassium delayed-rectifier current

$$\begin{aligned} I_{\mathrm{K}} &= \bar{g}_{\mathrm{K}} n^4 (V - E_{\mathrm{K}}) \\ \dot{n} &= \alpha_n(V)(1-n) - \beta_n(V) n \end{aligned}$$

$\bar{g}_{\mathrm{K}} = 36\,\mathrm{mS/cm^2}$, $E_{\mathrm{K}} = -77\,\mathrm{mV}$,
$\alpha_n(V) = 0.01(V+55)/(1-\exp(-(V+55)/10))$,
$\beta_n(V) = 0.125\exp(-(V+65)/80)$.

Leakage current

$$I_{\mathrm{L}} = \bar{g}_{\mathrm{L}}(V - E_{\mathrm{L}})$$

$\bar{g}_{\mathrm{L}} = 0.3\,\mathrm{mS/cm^2}$, $E_{\mathrm{L}} = -54.384\,\mathrm{mV}$.

6.2 Traub-Miles model

This model is a simple example of a class-I neuron (Traub et al., 1991). Note that it contains the same currents as the Hodgkin-Huxley model. Only their parameters are slightly changed. The resting potential is at $V = -66.6\,\mathrm{mV}$.

$$C\dot{V} = -I_{\mathrm{Na}} - I_{\mathrm{K}} - I_{\mathrm{L}} + I$$

Membrane capacitance: $C = 1\,\mu\,\mathrm{F/cm^2}$

Sodium current

$$\begin{aligned} I_{\mathrm{Na}} &= \bar{g}_{\mathrm{Na}} m^3 h (V - E_{\mathrm{Na}}) \\ \dot{m} &= \alpha_m(V)(1-m) - \beta_m(V) m \\ \dot{h} &= \alpha_h(V)(1-h) - \beta_h(V) h \end{aligned}$$

$\bar{g}_{\mathrm{Na}} = 100\,\mathrm{mS/cm^2}$, $E_{\mathrm{Na}} = +48\,\mathrm{mV}$,
$\alpha_m(V) = 0.32(V+54)/(1-\exp(-(V+54)/4))$,
$\beta_m(V) = 0.28(V+27)/(\exp((V+27)/5)-1)$,
$\alpha_h(V) = 0.128\exp(-(V+50)/18)$,
$\beta_h(V) = 4/(1+\exp(-(V+27)/5))$.

Potassium delayed-rectifier current

$$\begin{aligned} I_{\mathrm{K}} &= \bar{g}_{\mathrm{K}} n^4 (V - E_{\mathrm{K}}) \\ \dot{n} &= \alpha_n(V)(1-n) - \beta_n(V) n \end{aligned}$$

$\bar{g}_{\mathrm{K}} = 200\,\mathrm{mS/cm^2}$, $E_{\mathrm{K}} = -82\,\mathrm{mV}$,
$\alpha_n(V) = 0.032(V+52)/(1-\exp(-(V+52)/5))$,
$\beta_n(V) = 0.5\exp(-(V+57)/40)$.

Leakage current

$$I_{\mathrm{L}} = \bar{g}_{\mathrm{L}}(V - E_{\mathrm{L}})$$

$\bar{g}_{\mathrm{L}} = 0.1\,\mathrm{mS/cm^2}$, $E_{\mathrm{L}} = -67\,\mathrm{mV}$.

Deutschsprachige Zusammenfassung

Durch die Anwendung eines neuartigen Ansatzes ist es Gollisch et al. (2005) gelungen neue Einblicke in die Dynamik und Signalverarbeitung von auditorischen Rezeptorzellen zu liefern. In dieser Studie wurden mittels eines phänomenologischen Kaskadenmodells die linearen Filter und Nichtlinearitäten der auditorischen Signaltransduktion quantitativ allein aus der Kenntnis der Eingangsstimuli und der Ausgangs-Wahrscheinlichkeit, dass ein Aktionspotential (AP) ausgelöst wird, bestimmt. Die verwendete Methode beruht auf der Messung von sogenannten "Iso-Response"-Kurven, die in anderem Kontext in der Psychophysik (z.B. Isophone in der Auditorik) verwendet werden. Bei diesem Ansatz werden die Stimulus-Parameter $(s_1, s_2, \ldots, s_n)$ dergestalt verändert, dass der Output des Systems konstant bleibt. Die gemessenen Stimulus-Konstellationen stellen Invarianzen dar, die das System nicht unterscheiden kann und enthüllen bei geeigneter Wahl der Stimuli System-spezifische Eigenschaften. In der Studie von Gollisch et al. (2005) wurden Paare kurzer akustischer Impulse (A_1, A_2), sogenannte "Clicks", verwendet, die durch eine variable Zeit Δt getrennt sind. Die Amplituden der Impulse wurden so justiert, dass die Wahrscheinlichkeit ein Aktionspotential auszulösen bei konstant 70% liegt. Die zeitliche Auflösung der Methode ist nur durch die Präzision des Stimulus begrenzt (ca. 10μs), und damit um ein Vielfaches höher als die zeitliche Variabilität der APs (ca. 1 ms). Durch die Messung solcher "Iso-Response Sets" (IRS) für verschiedene Zeiten Δt kann auf diese Weise eine hochaufgelöste "Karte" der sogenannten "effektiven Stimulusstärke" erstellt werden. Mithilfe mehrerer solcher Datensätze für unterschiedliche Stimuli lassen sich die funktionalen Filtereigenschaften der auditorischen Signaltransduktion berechnen.

Diese Diplomarbeit beginnt mit einer Einleitung in den mathematischen Rahmen der Methode und setzt dann mit der Reproduktion der oben genannten Studie mit Hilfe numerischer Simulationen fort. Wir untersuchen, wie die Ergebnisse der IRS interpretiert werden müssen und stellen durch den Vergleich der Modelparameter mit den Messungen fest, dass nur ein Teil der effektiven Stimulusstärke durch die Methode erfasst wird. Die Begründung für diese Eigenschaft wird durch eine Untersuchung des mathematischen Rahmens der Methode geliefert. Wir zeigen dann auf, dass die Unterscheidung der linearen Filter des Kaskadenmodells darauf beruht, dass der Zeitverlauf des ersten linearen Filters kürzer ist als der des zweiten linearen Filters. Durch die Simulation von vollständigen AP-Generatoren, wie sie im Neuron z.B. am Axonhügel zu finden sind, zeigen wir, dass die Methode alle integrativen Eigenschaften des AP-Generators erfasst, sofern dessen Dynamik langsamer ist als die der vorangehenden Prozesse. In diesem Zusammenhang zeigen wir auch, das dass unter Umständen die Dynamik des Spike-Generators einen störenden Einfluss auf die Messung der Filtereigenschaften haben kann.

Weiterhin zeigen wir, dass die Messung einer anderen Art von IRS im "Amplituden-Raum" der Stimulus-Paare zu verschiedenen Δt keine eindeutige Einsicht in die Natur der Input-Nichtlinearität liefert.

Neben unseren Untersuchungen zur Interpretation von IRS, testen wir, ob es unter Umständen zu einer Trennung von funktionalen Filtermodulen durch den Einfluss von Rauschen kommt. Die von uns verwendeten Szenarien ergeben keine Hinweise auf ein solches Phänomen, so dass wir davon ausgehen müssen, dass alle Filtereigenschaften der zweiten Linearität des Kaskadenmodells durch die IRS erfasst werden.

Schließlich setzen wir die unsere Ergebnisse in einen größeren Zusammenhang und diskutieren welchen Aufschluss uns die IRS über tatsächlich bestehende biophysikalische Mechanismen gibt.

Bibliography

Andersen P, Raastad M, Storm JF (1990) Excitatory synaptic integration in hippocampal pyramids and dentate granule cells. *Cold Spring Harb Symp Quant Biol* 55: 81–86.

Brown TH, Fricke RA, Perkel DH Oct (1981) Passive electrical constants in three classes of hippocampal neurons. *J Neurophysiol* 46: 812–827.

Clements JD, Redman SJ Feb (1989) Cable properties of cat spinal motoneurones measured by combining voltage clamp, current clamp and intracellular staining. *J Physiol* 409: 63–87.

Eguíluz VM, Ospeck M, Choe Y, Hudspeth AJ, Magnasco MO May (2000) Essential nonlinearities in hearing. *Phys Rev Lett* 84: 5232–5235.

Fleshman J, Segev I, Burke R (1988) Electrotonic architecture of type identified α-motoneurons in the cat spinal cord. *J Neurophysiol* 60: 60–85.

French AS (1988) Transduction mechanisms of mechanosensilla. *Annu Rev Entomol* 33: 39–58.

Gentet LJ, Stuart GJ, Clements JD (2000) Direct measurement of specific membrane capacitance in neurons. *Biophysical Journal* 79: 314–320.

Gillespie PG (1995) Molecular machinery of auditory and vestibular transduction. *Curr Opin Neurobiol* 5: 449–455.

Gillespie PG, Walker RG (2001) Molecular basis of mechanosensory transduction. *Nature* 413: 194–202.

Gollisch T (2004) *The Auditory Transduction Chain.* PhD thesis Mathematisch-Naturwissenschaftliche Fakultaet I der Humboldt-Universitaet zu Berlin.

Gollisch T, Herz AVM (2005) Disentangling sub-millisecond processes within an auditory transductin chain. *PLoS Biol.* 3: e8.

Gollisch T, Schütze H, Benda J, Herz AVM (2002) Energy integration describes sound-intensity coding in an insect auditory system. *J Neurosci.* 22: 10434–10448.

Gray EG (1960) The fine structure of the insect ear. *Philos Trans R Soc London* 94: 243–275.

Hartwell LH, Hopfield JJ, Leibler S, Murray AW (1999) From molecular to modular cell biology. *Nature* 402: C47–C52.

Hill KG (1983) The physiology of locust auditory receptors. i. discrete depolarizations of receptor cells. *J Comp Physiol A* 152: 475–482.

Hodgkin AL, Huxley AF Apr (1952)a The components of membrane conductance in the giant axon of loligo. *J Physiol* 116: 473–496.

Hodgkin AL, Huxley AF Apr (1952)b Currents carried by sodium and potassium ions through the membrane of the giant axon of loligo. *J Physiol* 116: 449–472.

Hodgkin AL, Huxley AF Apr (1952)c The dual effect of membrane potential on sodium conductance in the giant axon of loligo. *J Physiol* 116: 497–506.

Hodgkin AL, Huxley AF Aug (1952)d A quantitative description of membrane current and its application to conduction and excitation in nerve. *J Physiol* 117: 500–544.

Hudspeth AJ Nov (1985) The cellular basis of hearing: the biophysics of hair cells. *Science* 230: 745–752.

Hudspeth AJ Oct (1989) How the ear's works work. *Nature* 341: 397–404.

Hudspeth AJ, Logothetis NK Oct (2000) Sensory systems. *Curr Opin Neurobiol* 10: 631–641.

Jacobs K, Otte B, Lakes-Harlan R (1999) Tympanal receptor cells of schistocerca gregaria: Correlation of soma positions and dendrite attachment sites, central projections and physiologies. *J Exp Zool* 283: 270–285.

Knudsen EI (1980) Sound localization in birds. In Popper AN, Fay RR, editors, *Comparative Studies of Hearing in Vertebrates* pages 289–322. Springer, New York.

Koch C, Rapp M, Segev I (1996) A brief history of time (constants). *Cerebral Cortex* 6: 93–101.

Kössl M, Boyan GS Mar (1998) Otoacoustic emissions from a nonvertebrate ear. *Naturwissenschaften* 85: 124–127.

Martin P, Hudspeth AJ Dec (1999) Active hair-bundle movements can amplify a hair cell's response to oscillatory mechanical stimuli. *Proc Natl Acad Sci U S A* 96: 14306–14311.

Martin C. Göpfert DR (2002) The mechanical basis of drosophila audition. *The Journal of Experimental Biology* 205: 1199–1208.

Martinac B (2001) Mechanosensitive channels in prokaryotes. *Cell Physiol Biochem* 11: 61–76.

Mason AC, Oshinsky ML, Hoy RR Apr (2001) Hyperacute directional hearing in a microscale auditory system. *Nature* 410: 686–690.

Michelsen A Sep (1966) Pitch discrimination in the locust ear: observations on single sense cells. *J Insect Physiol* 12: 1119–1131.

Michelsen A (1971)a The physiology of the locust ear. ii. frequency discrimination based upon resonance in the tympanum. *Z vergl Physiologie* 71: 63–101.

Michelsen A (1971)b The physiology of the locust ear. iii. acoustic properties of the intact ear. *Z vergl Physiologie* 71: 102–128.

Michelson A (1971) The physiology of the locust ear. i. frequency sensitivity of single cells in the isolated ear. *Z vergl Physiologie* 71: 49–62.

Neuweiler G, Schmidt S (1993) Audition in echolocating bats. *Curr Opin Neurobiol* 3: 563–569.

Nitzan R, Segev I, Yarom Y Feb (1990) Voltage behavior along the irregular dendritic structure of morphologically and physiologically characterized vagal motoneurons in the guinea pig. *J Neurophysiol* 63: 333–346.

Prinz P, Ronacher B Aug (2002) Temporal modulation transfer functions in auditory receptor fibres of the locust (locusta migratoria l.). *J Comp Physiol A Neuroethol Sens Neural Behav Physiol* 188: 577–587.

Rapp M, Segev I, Yarom Y Jan (1994) Physiology, morphology and detailed passive models of guinea-pig cerebellar purkinje cells. *J Physiol* 474: 101–118.

Reyes AD, Rubel EW, Spain WJ Sep (1994) Membrane properties underlying the firing of neurons in the avian cochlear nucleus. *J Neurosci* 14: 5352–5364.

Robles L, Ruggero MA Jul (2001) Mechanics of the mammalian cochlea. *Physiol Rev* 81: 1305–1352.

Russel IJ, Sellick PM (1983) Low-frequency characteristics of intracellularly recorded receptor potentials in guinea-pig cochlear hair cells. *J Physiol* 338: 179–206.

Smith CUM (2000) *Biology of Sensory Systems.* John Wiley & Sons Ltd.

Stephen RO, Bennet-Clark HC (1982) The anatomical and mechanical basis of stimulation and frequency analysis in the locust ear. *J Exp Biol* 99: 279–314.

Traub RD, Wong RK, Miles R, Michelson H (1991) A model of a ca3 hippocampal pyramidal neuron incorporating voltage-clamp data on intrinsic conductances. *Journal of Neurophysiology* 66(2): 635–650.

Zigmond MJ, Bloom FE, Landis SC, Roberts JL, Squire LR, editors (1999) *Fundamental Neuroscience.* Academic Press.